

# The CGM at Cosmic Noon with KCWI: Outflows from a Star-forming Galaxy at $z = 2.071$

NIKOLE M. NIELSEN <sup>1,2</sup> GLENN G. KACPRZAK <sup>1,2</sup> STEPHANIE K. POINTON <sup>1,2</sup> MICHAEL T. MURPHY <sup>1</sup>  
CHRISTOPHER W. CHURCHILL <sup>3</sup> AND ROMEEL DAVÉ <sup>4</sup>

<sup>1</sup>*Centre for Astrophysics and Supercomputing, Swinburne University of Technology, Hawthorn, Victoria 3122, Australia*

<sup>2</sup>*ARC Centre of Excellence for All Sky Astrophysics in 3 Dimensions (ASTRO 3D)*

<sup>3</sup>*Department of Astronomy, New Mexico State University, Las Cruces, NM, 88003, USA*

<sup>4</sup>*Institute for Astronomy, Royal Observatory, University of Edinburgh, Edinburgh EH9 3HJ, UK*

(Accepted October 26, 2020)

Submitted to ApJ

## ABSTRACT

We present the first results from our CGM at Cosmic Noon with KCWI program to study gas flows in the circumgalactic medium (CGM) at  $z = 2 - 3$ . Combining the power of a high-resolution VLT/UVES quasar spectrum, an *HST*/ACS image, and integral field spectroscopy with Keck/KCWI, we detected Ly $\alpha$  emission from a  $1.7L_*$  galaxy at  $z_{\text{gal}} = 2.0711$  associated with a Lyman limit system with weak MgII ( $W_r(2796) = 0.24 \text{ \AA}$ ) in quasar field J143040+014939. The galaxy is star-forming ( $\text{SFR}_{\text{FUV}} = 37.8 \text{ M}_{\odot} \text{ yr}^{-1}$ ) and clumpy: either an edge-on disk ( $i = 85^\circ$ ) or, less likely, a major merger. The background quasar probes the galaxy at an impact parameter of  $D = 66 \text{ kpc}$  along the projected galaxy minor axis ( $\Phi = 89^\circ$ ). From photoionization modeling of the absorption system, we infer a total line-of-sight CGM metallicity of  $[\text{Si}/\text{H}] = -1.5^{+0.4}_{-0.3}$ . The absorption system is roughly kinematically symmetric about  $z_{\text{gal}}$ , with a full MgII velocity spread of  $\sim 210 \text{ km s}^{-1}$ . Given the galaxy-quasar orientation, CGM metallicity, and gas kinematics, we interpret this gas as an outflow that has likely swept-up additional material. By modeling the absorption as a polar outflow cone, we find the gas is decelerating with average radial velocity  $V_{\text{out}} = 109 - 588 \text{ km s}^{-1}$  for half opening angles of  $\theta_0 = 14^\circ - 75^\circ$ . Assuming a constant  $V_{\text{out}}$ , it would take on average  $t_{\text{out}} \sim 111 - 597 \text{ Myr}$  for the gas to reach 66 kpc. The outflow is energetic, with a mass outflow rate of  $\dot{M}_{\text{out}} < 52 \pm 37 \text{ M}_{\odot} \text{ yr}^{-1}$  and mass loading factor of  $\eta < 1.4 \pm 1.0$ . We aim to build a sample of  $\sim 50$  MgII absorber-galaxy pairs at this epoch to better understand gas flows when they are most actively building galaxies.

**Keywords:** Galaxy evolution (594), High-redshift galaxies (734), Lyman-alpha galaxies (978), Quasar absorption line spectroscopy (1317), Circumgalactic medium (1879)

## 1. INTRODUCTION

One of the most challenging problems for deciphering how galaxies evolve is understanding how they obtain their gas and process it into stars. Simulations and simple models suggest that the baryon cycle, or the flow of gas onto, out of, and back onto galaxies, is the main regulator of star formation (e.g., Oppenheimer & Davé 2008; Lilly et al. 2013). We further know that the cosmic star formation rate peaks at  $z = 2 - 3$ , also known

as “Cosmic Noon,” when galaxies assemble roughly half of their stellar mass (Madau & Dickinson 2014). At this epoch, strong galactic outflows are regularly observed (e.g., Steidel et al. 2010; Rupke 2018) and simulations predict the rate of accretion is greatest (e.g., van de Voort et al. 2011). As a result, Cosmic Noon is the ideal epoch for studying the baryon cycle. The ideal location for this study is the circumgalactic medium (CGM; Tumlinson et al. 2017), which is generally defined as the bound gaseous halo around galaxies. Accreting gas from the intergalactic medium (IGM) to the interstellar medium (ISM) must first pass through the CGM, which is also where most outflowing gas is deposited.

The CGM is therefore the record-keeper of past gas flows and a reservoir for future star formation.

At low redshift,  $z \lesssim 1$ , we now understand that the CGM is massive, containing a gas mass at least comparable to the gas mass within galaxies themselves (Thom et al. 2011; Tumlinson et al. 2011; Werk et al. 2013), and holds a substantial fraction of baryons (e.g., Peebles et al. 2014; Werk et al. 2014). Quasar absorption line spectroscopy has shown that this multiphase gas is accreting/rotating (e.g., Kacprzak et al. 2010a, 2019b; Nielsen et al. 2015; Ho et al. 2017; Ho & Martin 2020; Zabl et al. 2019) and outflowing (e.g., Kacprzak et al. 2014, 2019b; Muzahid et al. 2015; Nielsen et al. 2015; Schroetter et al. 2016, 2019; Martin et al. 2019). These gas flows are likely confined to the projected major and minor axes of their host galaxies, respectively (Bordoloi et al. 2011; Bouché et al. 2012; Kacprzak et al. 2012, 2015a; Lan et al. 2014; Lan & Mo 2018; Schroetter et al. 2019), and there is evidence that their metallicities are bimodal (at least for partial Lyman limit systems and Lyman limit systems, pLLSs/LLSs, at  $0.45 < z < 1.0$ ; Lehner et al. 2013, 2019; Wotta et al. 2016, 2019). One might then assume that there should be two clear populations of gas on the azimuthal angle–CGM metallicity plane. Recent work by Pointon et al. (2019) suggests that this simple model of metal-poor accretion along the projected major axis and metal-rich outflows along the projected minor axis is not clearly observed. Furthermore, comparing the CGM metallicity to the galaxy ISM metallicity does not seem to improve the situation, where the gas flow metallicities still have a wide range of values compared to the host galaxies regardless of the azimuthal angle (Péroux et al. 2016; Kacprzak et al. 2019a). It is possible that this experiment simply needs a larger sample to detect this bimodality (e.g., Péroux et al. 2020) or the metallicity analysis needs to account for dust (e.g., Wendt et al. 2020). Alternatively, since gas flows are likely diminishing in strength from Cosmic Noon towards present day, we might expect their signatures to be weaker and more well-mixed at low  $z$ , resulting in a lack of a metallicity difference for the observed gas flows (e.g., Hafen et al. 2017, 2019; although Péroux et al. 2020 suggest that there may not be a metallicity–azimuthal angle bimodality at high redshift). The next frontier for this sort of investigation is then high redshift.

Up until recently obtaining a large sample of absorber–galaxy pairs was a time-intensive activity. Now the newest powerful method for studying the CGM in detail is integral field spectroscopy. VLT/MUSE campaigns are quickly building large samples of absorber–galaxy pairs with a field-of-view of  $1''$ , covering a wide redshift range below  $z < 1.5$  and above  $z > 3$ . At low

redshift, these campaigns find galaxies hosting CGM absorption (e.g., Schroetter et al. 2019; Dutta et al. 2020), detect faint galaxies near CGM host galaxies that were previously thought to be isolated (e.g., Péroux et al. 2017; Rahmani et al. 2018; Hamanowicz et al. 2020), easily obtain two dimensional information about all galaxies in the fields for morphology and kinematic analyses (e.g., Schroetter et al. 2016, 2019; Zabl et al. 2019), and allow for multiple probes of the CGM hosted by a single galaxy using multiple background galaxies (e.g., Péroux et al. 2018) or even single background lensed galaxies (e.g., gravitational-arc tomography; Lopez et al. 2018, 2020). At the moment, MUSE cannot reach the epoch at which galaxies are most actively building up their mass,  $z = 2 - 3$ , because it does not yet have the spectral coverage required.

The Keck Baryonic Structure Survey (KBSS; Rudie et al. 2012) is currently the largest survey of  $z = 2 - 3$  CGM absorber–galaxy pairs, where they have obtained galaxy redshifts using multi-object spectroscopy on Keck/MOSFIRE. By studying the redshift space distortions around these galaxies, the KBSS have found enhancements of metal lines out to 180 kpc and  $\sim 240 - 350 \text{ km s}^{-1}$ , which were interpreted as inflows (Turner et al. 2014, 2017) and hot, metal-enriched outflows (Turner et al. 2015). Neutral hydrogen also has significant enhancements in redshift space distortions, where Chen et al. (2020) stacked several thousand foreground–background galaxy pairs and suggested that outflows dominate HI kinematics up to 50 kpc from galaxies but inflows dominate beyond 100 kpc. Rudie et al. (2019) studied the multiphase CGM of eight galaxies, finding substantial metal reservoirs ( $> 25\%$  of the ISM metal mass), complex kinematics, unbounded gas, and high covering fractions ( $> 50\%$ ). These characteristics point to outflowing gas and a dynamic CGM, where both heating and cooling processes occur often. To better understand the source of the observed absorption, two key pieces of information that are important for enhancing our insights are absent from the KBSS: CGM metallicities and galaxy morphologies.

A few  $z = 2 - 3$  absorber–galaxy pairs have galaxy morphologies and CGM metallicities. These include the damped Ly  $\alpha$  (DLA) absorbers from Bouché et al. (2013) and Krogager et al. (2013). Both DLAs are metal-rich for  $z = 2 - 3$  systems (e.g., Lehner et al. 2016), but are located along the major and minor axes, respectively. Bouché et al. (2013) concluded that the major axis DLA was consistent with a coplanar gaseous accretion disk since the gas metallicity was significantly lower than the galaxy ISM metallicity and the kinematics pointed to a combination of accretion and rotating disk components.

Krogager et al. (2013) concluded that the minor axis DLA probed outflowing gas based on its location about the galaxy and high metallicity, but did not model the kinematics. An important caveat to these results is that both absorber–galaxy pairs have very low impact parameters of 26 and 6 kpc, respectively, and are likely tracing some component of an extended galaxy disk itself.

Even without galaxy morphologies, CGM metallicities have proven useful for better constraining the gas flow origins at high redshift. Crighton et al. (2015) studied a  $z \sim 2.5$  pLLS, finding metal-enriched clouds with a large velocity width. The authors concluded that the gas was consistent with an outflowing wind if they assumed the host was an edge-on galaxy probed along the projected minor axis. More confidently confirming this scenario requires modeling the galaxy morphology and gas kinematics. Zahedy et al. (2019b) found several Ly $\alpha$  emitters at  $z \sim 2.8$  associated with strong Ly $\alpha$  absorption in a background quasar spectrum with metallicities as low as  $\sim 0.01 - 0.001$  solar, which is consistent with the level of enrichment in the IGM at this redshift. The authors suggested these low mass Ly $\alpha$  emitters were therefore embedded in an IGM accretion stream.

Building up a large sample of absorber–galaxy pairs at Cosmic Noon surrounding a variety of galaxies is important for studying these gas flows during a highly influential epoch in the Universe’s history. Here we present the first results from our CGM at Cosmic Noon with KCWI program. This paper is organized as follows. Section 2 details the observations and analysis methods for the quasar spectra, *HST* images, and IFU spectroscopy. Section 3 presents the CGM of a host galaxy at  $z \sim 2$ , characterizes the CGM metallicities and kinematics, and explores an outflowing wind as the origin of the observed gas. Section 4 places the results in the context of Cosmic Noon star formation-driven outflows and other possible mechanisms that could give rise to the absorbing gas. Finally, Section 5 summarizes and concludes our first study with KCWI at Cosmic Noon. Throughout the paper we report AB magnitudes, physical distances, and adopt a  $\Lambda$ CDM cosmology ( $H_0 = 70 \text{ km s}^{-1} \text{ Mpc}^{-1}$ ,  $\Omega_M = 0.3$ , and  $\Omega_\Lambda = 0.7$ ).

## 2. OBSERVATIONS AND METHODS

Our CGM at Cosmic Noon with KCWI program is designed to obtain  $\sim 50$  MgII absorber–galaxy pairs with the following considerations. We compiled a sample of quasar fields with known MgII absorption at  $1.9 < z_{\text{abs}} < 2.6$ , where each field has been imaged with *HST* (ACS, WFPC2, and/or WFC3) or Keck (NIRC2 with laser guide star adaptive optics) and high-resolution quasar spectra are available from VLT/UVES and/or

HIRES/Keck. The quasar spectra are sourced from KODIAQ DR1 (O’Meara et al. 2015), SQUAD DR1 (Murphy et al. 2019), or Evans (2011, also see Churchill et al. 2020). The latter quasar sample includes many quasars that are listed in KODIAQ DR2 (O’Meara et al. 2017). The absorbers were drawn from the Mathes et al. (2017) and Hasan et al. (2020) sample, where MgII and CIV absorption were systematically and automatically searched using a matched-filter analysis similar to Zhu & Ménard (2013) and then later visually confirmed.

For each field in our program, multiple  $z \sim 2$  MgII and CIV absorbers have been identified at  $z_{\text{abs}} < z_{\text{qso}} - (1 + z_{\text{qso}})(3000 \text{ km s}^{-1}/c)$  to avoid systems associated with the quasar. We have placed no restrictions on the measured equivalent width of the MgII and CIV lines other than the requirement that they be detected at the  $5\sigma$  level. Finally, we had no a priori knowledge of the host galaxy properties (i.e., galaxies were not yet identified). With this information in-hand, we have thus far observed 15 fields with the Keck Cosmic Web Imager (KCWI; Morrissey et al. 2018) on Keck II, corresponding to 30 MgII and 80 CIV absorbers, searching for Ly $\alpha$  emission from galaxies at Cosmic Noon. While this sample is initially MgII absorption-selected, the IFU nature of KCWI allows us to identify *all*  $z \sim 2$  galaxies within the field of view of the instrument. We expect to identify at least as many MgII non-absorbing galaxies as MgII absorbing galaxies. In particular, a majority of the 80 CIV absorbers we have covered in the sample do not have measurable MgII absorption.

Here we present the first result from our program: a MgII absorber–galaxy pair at  $z = 2.071$  in quasar field J143040+014939 (hereafter J1430+014).

### 2.1. Quasar Spectroscopy and Photoionization Modeling

Quasar J1430+014,  $z_{\text{qso}} = 2.119$  was observed with VLT/UVES for a total of 15077 s (PIDs 079.A-0656(A) and 081.A-0478(A)). The spectrum was reduced with the UVES pipeline (Dekker et al. 2000) and exposures were combined and continuum fit with UVES-POPLER (Murphy 2016; Murphy et al. 2019). During this process, the wavelengths were vacuum and heliocentric velocity corrected. The spectrum covers multiple lines for the  $z_{\text{abs}} = 2.0708$  absorber such as Ly $\alpha$ , MgII, and CIV, which are further described in Section 3.2.

With these data, the absorption system was characterized using the methods presented in Pointon et al. (2019). In short, absorption profiles were modeled with VPFIT (Carswell & Webb 2014) to obtain equivalent widths, column densities, and the kinematic structure. Upper limits on equivalent width and column density

( $3\sigma$ ) were measured by assuming a single cloud with a Doppler parameter of  $b \sim 8 \text{ km s}^{-1}$ . As shown in Section 3.2, the upper limits on absorption are located on the linear or near-linear part of the curve-of-growth, thus the equivalent width limit is not sensitive to the choice of Doppler parameter. The absorption redshift,  $z_{\text{abs}}$ , is defined as the optical depth-weighted median of absorption for MgII.

The total measured column densities, measured by summing the column densities of the fitted Voigt profile (VP) components, were then compared to the predicted column densities generated by CLOUDY (Ferland et al. 2013) to infer the total line-of-sight CGM metallicity. CLOUDY generates column density predictions given HI column densities ( $N_{\text{HI}}$ ), hydrogen densities ( $n_{\text{H}}$ ), and metallicities ( $[\text{Si}/\text{H}]$ ) by modeling a uniform layer of gas that is irradiated by background UV radiation. Here we use the updated Haardt & Madau (2001) UV background (HM05 in CLOUDY) for comparison to low redshift work. The more recent HM12 UV background (Haardt & Madau 2012) is a harder spectrum, resulting in higher metallicity estimates with a dependence on HI column density at low redshift (Chen et al. 2017; Wotta et al. 2019; Zahedy et al. 2019a). While the results using HM12 are also reported here for completeness, we focus on the HM05 results for direct comparison to the large body of CGM metallicity work using HM05 and to prevent any systematic biases that may be present when comparing the results of the different UV backgrounds. We assumed a single-phase model with no dust and with a solar abundance pattern (Crighton et al. 2013, 2015, 2016). This single-phase model forces the assumption that the majority of HI is associated with the low and intermediate ionization ions and this assumption is widely used (e.g., Cooper et al. 2015; Fumagalli et al. 2016; Lehner et al. 2016, 2019; Wotta et al. 2016, 2019; Prochaska et al. 2017; Pointon et al. 2019, 2020). Studying the multiphase and multi-component nature of CGM absorbers suggests that this assumption is valid, where Muzahid et al. (2015) found that HI is predominantly associated with the low ionization phase, with small contributions from the high ionization phase. We then constructed a likelihood function using the measured column densities including upper limits and CLOUDY grids. Priors on the column densities were applied and we used a Markov chain Monte Carlo (MCMC) analysis with Bayesian statistics following the Crighton et al. (2015) methods with emcee (Foreman-Mackey et al. 2013) to generate posterior distributions for  $N_{\text{HI}}$ ,  $n_{\text{H}}$ ,  $U$ , and  $[\text{Si}/\text{H}]$ . Metallicities are reported as  $[\text{Si}/\text{H}]$  for comparison to low redshift. Further details are presented in Section 3.3.

## 2.2. *HST* Imaging and Galaxy Morphologies

The field was imaged with *HST* using the F625W filter on the ACS for 700 s (PID: 10576) and the data were reduced using the DrizzlePac software (Gonzaga et al. 2012). We used the Source Extractor software (SExtractor; Bertin & Arnouts 1996) to measure the galaxy photometry with a detection criterion of  $1.5\sigma$  above the background. The resulting magnitude is quoted in the AB system. The *HST* image centered on J1430+014 is shown in the left panel of Figure 1.

Galaxy morphological parameters and orientations are modeled from the *HST* image following the methods of Kacprzak et al. (2015a). In summary, point spread functions (PSFs) for ACS images depend on both time and position on the chip and the images also contain significant geometrical distortions. Thus PSFs generated using Tiny Tim (Krist et al. 2011) are appropriate for each galaxy in the field and are then used in the galaxy modeling. Galaxy morphological parameters were quantified by fitting a two-component disk+bulge model using GIM2D (Simard et al. 2002). A disk component has an exponential profile while the bulge has a Sérsic profile with  $0.2 \leq n \leq 4.0$ . In order to quantify the location of the line-of-sight through the CGM relative to the modeled galaxy’s on-the-sky orientation, we adopt the standard convention that an azimuthal angle of  $\Phi = 0^\circ$  is defined as the background quasar is located along the galaxy projected major axis, while  $\Phi = 90^\circ$  is along the galaxy projected minor axis. Additionally, a face-on galaxy is defined as having an inclination of  $i = 0^\circ$ , while an edge-on galaxy has  $i = 90^\circ$ . Further details are discussed in Section 3.1.

## 2.3. *KCWI* Integral Field Spectroscopy

Keck/KCWI observations of the J1430+014 field were conducted on 2018 February 15 UT (PID: 2018A\_W185) with the medium image slicer and BL grating using a central wavelength of  $4500 \text{ \AA}$  and  $2 \times 2$  binning. The medium slicer has a field of view (FOV) of  $16''.5 \times 20''.4$ , resulting in a spatial sampling of  $0''.29 \times 0''.69$ , corresponding to  $2.4 \times 5.8 \text{ kpc}$  at  $z \sim 2$ . The BL grating has a spectral resolution of  $R \approx 1800$  ( $\sim 0.625 \text{ \AA pix}^{-1}$ ) and spans  $3500 \lesssim \lambda \lesssim 5500 \text{ \AA}$  for our central wavelength setting. Four exposures of 1300 s each (1.4 hrs total) were obtained on a single pointing with a position angle of  $0^\circ$ . The KCWI footprint is shown as the white rectangle on the *HST*/ACS image in the left panel of Figure 1. A single pointing was used in this field to maximize the amount of time spent on galaxies observable in the *HST*/ACS image. If a galaxy is not seen in the ACS image, then its morphology cannot be measured, especially since the KCWI spaxel sizes are on the order



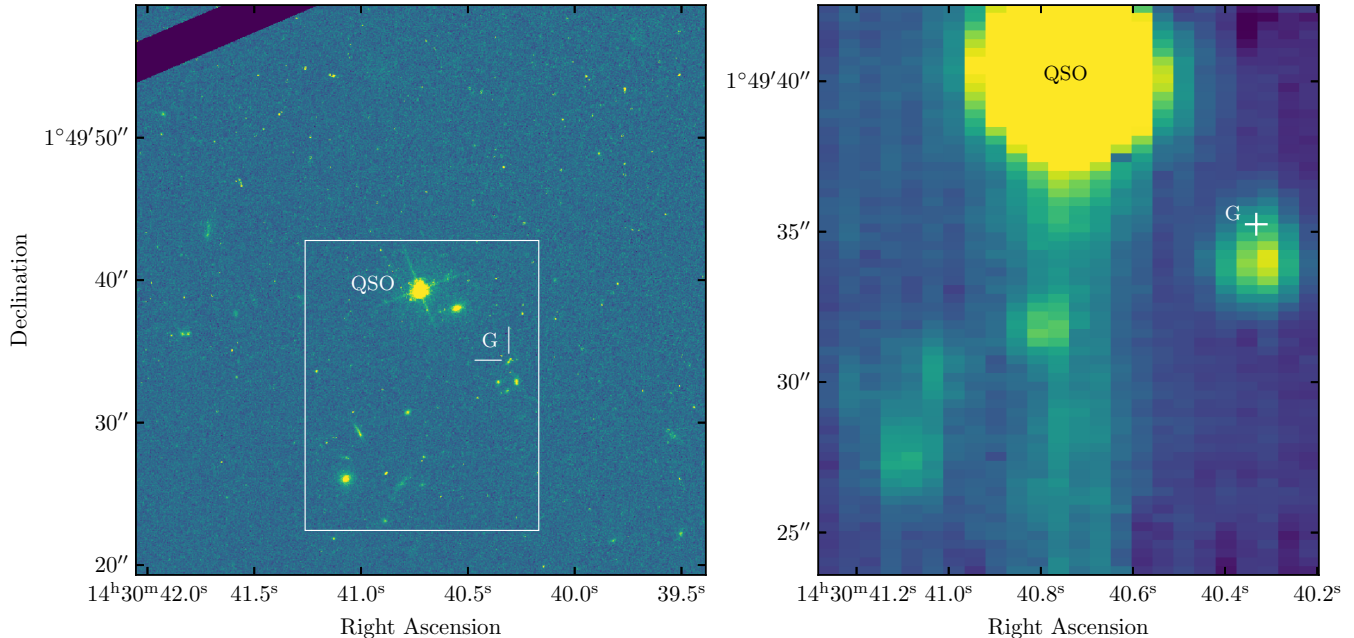


**Figure 1.** Overview of the quasar field J1430+014. (left) *HST*/ACS F625W image centered on the quasar. The KCWI field of view with the medium IFU slicer is marked with the white rectangle. (right) KCWI whitelight image, where the spectral direction is summed for each spaxel. The quasar (QSO) is the brightest object in both panels and the host galaxy (G) is marked by the cross. North is up and East is to the left in all images.

of  $z \sim 2$  galaxy sizes (half-light radii of  $\sim 2.5 - 3$  kpc; Allen et al. 2017). We have tiled around the quasar in the rest of our fields to obtain a better census of host galaxies.

The data were reduced using the publicly available KCWI Data Reduction Pipeline<sup>1</sup> using default settings. Since separate sky fields were not obtained, we masked the quasar, continuum objects, and any bright emission lines for the automated sky subtraction step so that the sky estimate is not skewed. Importantly, if the quasar is not removed before this step, then its spectrum is over-subtracted from the datacube resulting in false emission lines at wavelengths corresponding to strong intervening absorption observed in the quasar spectrum. The data were also flux-calibrated with standard star g191b2b from the KCWI DRP starlist. Finally, wavelengths were vacuum and heliocentric velocity corrected for direct comparison to the UVES quasar spectrum and the four exposures were combined. The final datacube has a  $3\sigma$  flux limit of  $3 \times 10^{-19}$  erg s $^{-1}$  cm $^{-2}$  Å $^{-1}$ .

The resulting KCWI whitelight image, where the wavelength axis has been collapsed, is shown in the right panel of Figure 1. The quasar is the brightest object in the field and several continuum objects are observed corresponding to galaxies in the *HST* image. Figure 2

presents the quasar spectrum extracted from the KCWI datacube over 32 spaxels. The black and green lines represent the data and error spectrum, respectively. The error spectrum has been multiplied by 20 in order to better show the variation across the spectrum. The purple annotations indicate absorption features associated with the  $z_{\text{abs}} = 2.0708$  MgII and CIV absorbers found in the VLT/UVES spectrum. Additionally, Ly $\alpha$  absorption is clearly observed in the KCWI quasar spectrum, providing a reference for host galaxy Ly $\alpha$  emission features with similar resolution.

### 3. RESULTS

In this section, we present the first results of our CGM at Cosmic Noon with KCWI program for J1430 + 014,  $z_{\text{abs}} = 2.0708$ . In this field, we search for and find the absorbing host galaxy, characterize the galaxy’s photometric properties, measure the absorption properties, estimate the CGM metallicity, and model the observed gas as outflowing material.

#### 3.1. Host Galaxy

To find the absorber host galaxy, we searched a narrow band of  $v = \pm 1000$  km s $^{-1}$  around the absorber redshift for Ly $\alpha$  emission. Figure 3 presents the results of this search, where the left panel shows the KCWI narrow band image. The quasar is the brightest source in the field and the host galaxy Ly $\alpha$  emission is located  $\theta = 7''.9$

<sup>1</sup> <https://github.com/Keck-DataReductionPipelines/KcwiDRP>

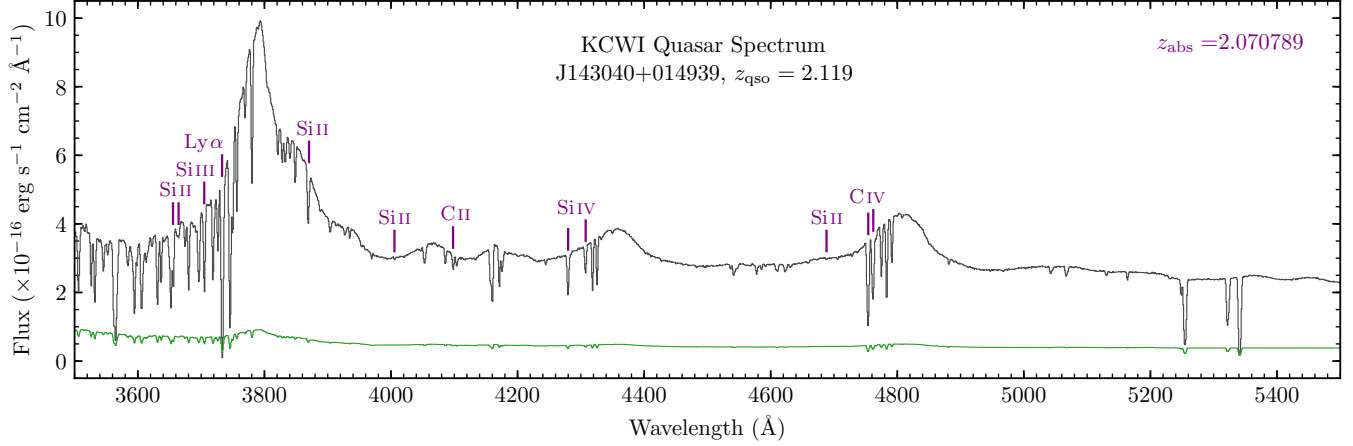


**Figure 2.** KCWI quasar spectrum with the BL grating for J1430+014 summed over 32 spaxels. The data are plotted as the black histogram and the associated uncertainty (multiplied by 20) is plotted as the green line. Purple ticks and labels indicate the detected absorption features associated with the  $z_{\text{abs}} = 2.0708$  absorption system. Further ions such as MgII and FeII are covered in the higher resolution VLT/UVES spectrum and all ions used in the metallicity analysis are plotted in Figure 5.

southwest of the quasar. The bright knot of emission corresponds to the galaxy from the *HST*/ACS image shown in the top right panel. No obvious emission from other galaxies in the *HST* image is observed in this field out to  $D < 150$  kpc.

The galaxy Ly $\alpha$  emission and CGM Ly $\alpha$  absorption from the quasar spectrum, both of which are 1D extracted spectra from the KCWI cube, are presented in the bottom right panels of Figure 3 (see Figure 4 for the full galaxy spectrum). The velocity zero point corresponds to the optical depth-weighted median of MgII absorption in the UVES spectrum. We selected 12 spaxels around the galaxy for extraction, which roughly corresponds to the full width of the seeing (FWHM  $\sim 1''$ ), and these spaxels are indicated by the white box in the left panel of Figure 3. Because Ly $\alpha$  emission is subject to resonant scattering and thus the profile depends on the amount and kinematics of gas the photons must pass through, the observed redshift is not necessarily the systemic galaxy redshift (e.g., Zheng & Miralda-Escudé 2002; Shapley et al. 2003; Rakic et al. 2011; Trainor et al. 2015). Therefore, we use the Method 2 red peak relation described in Verhamme et al. (2018),  $v_{\text{red}} = 0.8 \times \text{FWHM}(\text{Ly}\alpha) - 34 \text{ km s}^{-1}$ , to calculate the corrected galaxy redshift. We first obtain the observed Ly $\alpha$  emission wavelength by fitting a double Gaussian profile (purple line in the middle right panel of Figure 3) and finding the wavelength corresponding to the max flux of the line,  $\lambda_{\text{obs}} = 3736.79 \text{ Å}$ . This wavelength is indicated in the panel by a vertical red dotted line. The full width at half maximum of this galaxy’s Ly $\alpha$  emission line is then  $\text{FWHM}(\text{Ly}\alpha) = 341 \text{ km s}^{-1}$ , which results in a redshifted velocity offset of  $v_{\text{red}} = 273 \text{ km s}^{-1}$  from

**Table 1.** Host Galaxy Properties

Property	Value	Units
RA	14:30:40.30	
Dec	+01:49:34.33	
$z_{\text{gal}}^a$	$2.0711 \pm 0.0008$	
$D$	$66.4 \pm 0.3$	kpc
$m_{\text{F625W}}$	$24.0 \pm 0.4$	AB mag
$M_B$	$-22.7^{+0.7}_{-0.8}$	
$L_B/L_B^*$	$1.7^{+1.9}_{-0.9}$	
$W_r(\text{Ly}\alpha)$	44.4	Å
$L_{\text{Ly}\alpha}$	$2.32 \times 10^{42}$	erg s $^{-1}$
$\text{SFR}_{\text{FUV}}$	37.8	$M_{\odot} \text{ yr}^{-1}$
$\text{SFR}_{\text{Ly}\alpha}^b$	$> 8.4$	$M_{\odot} \text{ yr}^{-1}$
$i^c$	$85^{+5}_{-2}$	degrees
$\Phi$	$89^{+1}_{-5}$	degrees

<sup>a</sup>We shifted the galaxy redshift blueward by  $v_{\text{red}} = 273 \text{ km s}^{-1}$  from  $\lambda_{\text{obs}} = 3736.79 \text{ Å}$  due to resonant scattering using:  $z_{\text{gal}} = z_{\text{Ly}\alpha} - (v_{\text{red}}/c)(\lambda_{\text{obs}}/1215.67)$ .

<sup>b</sup>Assuming  $f_{\text{esc,LyC}} = 0.0$  as a conservative lower limit. If we assume  $f_{\text{esc,LyC}} = 0.15$ , we measure  $\text{SFR}_{\text{Ly}\alpha} = 15.8 M_{\odot} \text{ yr}^{-1}$ .

<sup>c</sup>The galaxy is assumed to be a single clumpy galaxy rather than a major merger. See Section 4.1 for further discussion.

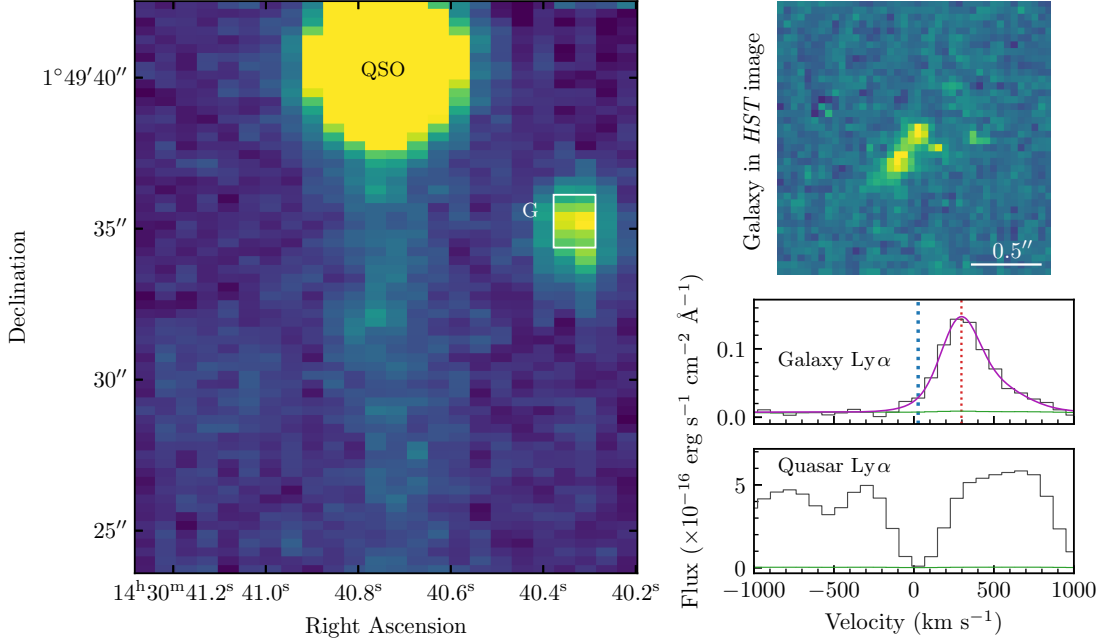


**Figure 3.** The galaxy associated with the observed absorption is located at  $D = 66$  kpc from the quasar sightline at  $z_{\text{gal}} = 2.0711$ . (left) KCWI slice within  $v \pm 1000$  km s $^{-1}$  of the Ly $\alpha$  absorption. The quasar (QSO) is the bright object at the top of the field of view, while the host galaxy (G) is the bright region 7 $''$ .9 away to the right side of the field of view. (upper right) The galaxy in the *HST* image, which is best modeled with an edge-on inclination ( $i = 85^{\circ} +5_{-2}$ ). The quasar sightline is oriented along the projected minor axis of the galaxy ( $\Phi = 89^{\circ} +1_{-5}$ ). (middle right) The galaxy Ly $\alpha$  emission line in the KCWI datacube summed over 12 spaxels (white box in the left panel). A double Gaussian fit is plotted as the purple curve. The wavelength at which the line peaks in flux measured from the Gaussian fit is plotted as the vertical red densely-dotted line while the final adopted galaxy redshift,  $z_{\text{gal}}$ , is plotted as the vertical blue loosely-dotted line. (bottom right) Ly $\alpha$  absorption in the KCWI quasar spectrum over 32 spaxels for reference. The velocity zero point corresponds to the  $z_{\text{abs}}$  measured from MgII absorption in the VLT/UVES quasar spectrum (see Figure 5).

the actual systemic galaxy redshift. This velocity was then applied with:  $z_{\text{gal}} = z_{\text{Ly}\alpha} - (v_{\text{red}}/c)(\lambda_{\text{obs}}/1215.67)$ . With this correction, we find that the host galaxy is located at  $z_{\text{gal}} = 2.0711 \pm 0.0008$  and this is plotted as the vertical blue dotted line in the middle right panel of Figure 3.

Full host galaxy properties are tabulated in Table 1. The galaxy is located at an impact parameter of  $D = 66$  kpc from the quasar sightline, which is reasonable compared to low redshift MgII samples. We converted the apparent magnitude,  $m_{\text{F625W}}$ , to an absolute  $B$ -band magnitude with a  $k$ -correction that assumes an Scd galaxy spectral energy distribution (e.g., Nielsen et al. 2013b) and report uncertainties corresponding to values derived using Sbc and Im galaxy SEDs in the Table. The absolute magnitude is then  $M_B = -22.7$ , corresponding to  $L_B/L_B^* = 1.7$  using the relation between  $M^*$  and redshift from Gabasch et al. (2004), which measures  $B$ -band luminosity functions over the range  $0.5 < z < 5.0$ .

From an inspection of the *HST* image, it is clear that the galaxy has a clumpy morphology, with a bright region on both sides of a disk-like structure. Galaxies

at  $z > 1$  typically have clumpy morphologies due to large star-forming regions observed at rest-frame UV wavelengths (i.e., the F625W band in Figure 1) and these irregular morphologies may be indistinguishable from mergers. The galaxy is similar to “double” or “chain” clump morphologies found in deep ( $\sim 100,000$  s) *HST*/ACS rest-frame UV images in the Hubble Ultra Deep Field (e.g., Elmegreen et al. 2007). Because of the short (700 s) exposure in the F625W band (rest-frame UV) of the J1430+014 field, it is not immediately clear if this galaxy is a clumpy edge-on disk or two small spheroidal galaxies undergoing a major merger. The major merger scenario appears to be less likely for the following reasons: 1) The object size is on the order of typical  $z = 2$  star-forming galaxy sizes ( $\sim 2.5 - 3$  kpc; van der Wel et al. 2014; Allen et al. 2017) but the clumps have a smaller separation, suggesting that a single object is more likely. 2) Quiescent galaxies are on average smaller, with sizes that are more consistent with the clump sizes in this object (van der Wel et al. 2014), but the object is star-forming as indicated by the presence of Ly $\alpha$  and the discussion later in this section. Thus

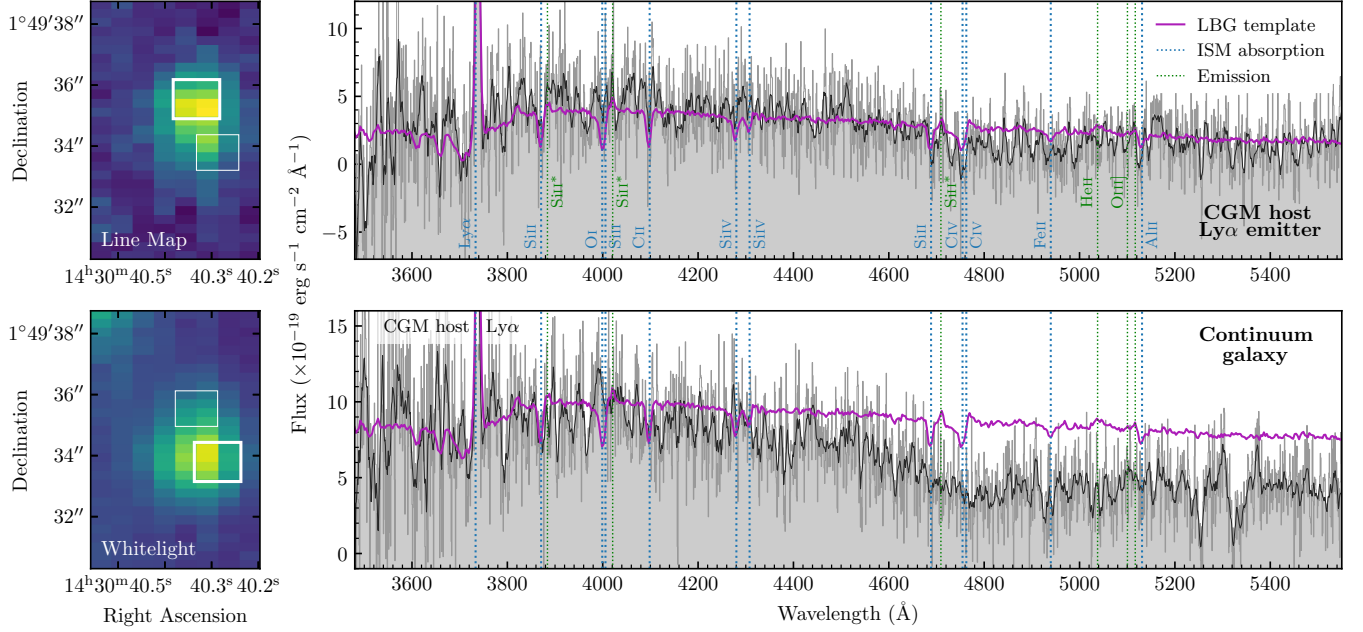


**Figure 4.** Comparison between the  $\text{Ly}\alpha$  emitting host galaxy (top) and an unrelated bright continuum galaxy contaminated with  $\text{Ly}\alpha$  emission (bottom). Left panels are a zoom-in view of the KCWI datacube, where the top image is a line map centered on  $v \pm 1000 \text{ km s}^{-1}$  around  $z_{\text{abs}}$  (see Figure 3). The bottom slice shows the bright continuum source which is physically offset from the  $\text{Ly}\alpha$  emission by  $\sim 1''.6$  (see Figure 1). Thick white boxes indicate the spaxels used to create the corresponding spectra on the right, while the thin white boxes are plotted for comparison. The spaxels chosen are offset slightly to reduce the amount of cross-contamination in the spectra. (right) The thin black lines are the data summed over eight spaxels in the KCWI datacube and the shaded region is plotted for ease in identifying absorption features. Both spectra have been smoothed using a boxcar filter over eight spectral pixels (thick black line). The Lyman break galaxy template from Shapley et al. (2003) is plotted in purple, where the wavelengths are shifted according to  $z_{\text{gal}} = 2.0711$  and the flux is adjusted to roughly match the flux surrounding the  $\text{Ly}\alpha$  emission line. Vertical dotted lines indicate strong ISM absorption and emission lines in the LBG template. The CGM host galaxy is well-fitted by a LBG template, whereas the continuum galaxy lacks the ISM absorption features required to classify as a  $z \sim 2$  LBG and the low continuum level at higher wavelengths indicates this is a lower redshift object. Thus the  $\text{Ly}\alpha$  emission in the bottom panel is likely contamination from the CGM host galaxy.

the quiescent galaxy sizes are not relevant here. 3) The probability of a galaxy at  $z = 2$  having a companion within a projected separation of  $0''.23$  or  $1.9 \text{ kpc}$ , which is the separation of the two clumps in our object, is  $0 - 3\%$  for galaxies in the Illustris simulations (Simons et al. 2019). Our full rationale for a single, clumpy galaxy assumption is discussed in Section 4.1. For the rest of our analysis, we assume the object is a single, clumpy galaxy that is not undergoing a major merger.

From the GIM2D modeling described in Section 2.2, we find that this object, assuming it is a single clumpy galaxy, is best modeled as an edge-on galaxy with  $i = 85^\circ$ . The modeling also indicates that the quasar sight-line probes the projected minor axis of this galaxy with  $\Phi = 89^\circ$ . Observations and simulations suggest that outflowing gas is primarily observed as bipolar cones aligned with the minor axis of galaxies (e.g., Veilleux et al. 2005; Bordoloi et al. 2011; Bouché et al. 2012; Kacprzak et al. 2012, 2014; Martin et al. 2012, 2019; Rubin et al. 2010, 2014; Shen et al. 2013; Fox et al.

2015; Schroetter et al. 2016; Nelson et al. 2019). Thus, assuming an edge-on morphology, this galaxy presents an ideal case for studying outflows in the CGM at peak star formation activity.

We measure a star formation rate (SFR) using two methods. The first method uses the relation between  $\text{Ly}\alpha$  luminosity and equivalent width presented in Sobral & Matthee (2019), who showed that  $\text{SFR}_{\text{Ly}\alpha}$  can be measured from this relation over a wide redshift range ( $0 < z < 2.6$ ) and is consistent with dust-corrected  $\text{H}\alpha$  SFRs. This method assumes a Salpeter IMF and a case B recombination ratio between  $\text{Ly}\alpha$  and  $\text{H}\alpha$ , but we convert to a Kroupa IMF by multiplying by  $0.62$  (e.g., Speagle et al. 2014). We obtain  $\text{SFR}_{\text{Ly}\alpha} = 8.4 \pm 0.8 \text{ M}_\odot \text{ yr}^{-1}$  by assuming  $f_{\text{esc,LyC}} = 0.0$ , the escape fraction of Lyman continuum photons. The value used for  $f_{\text{esc,LyC}}$  does affect the SFR, with larger escape fractions resulting in larger SFRs, but a value of  $0.0$  is typically assumed (Sobral & Matthee 2019), providing a conservative lower limit. If we use  $f_{\text{esc,LyC}} = 0.15$ , then



$\text{SFR}_{\text{Ly}\alpha} = 15.8 \pm 1.3 \text{ M}_{\odot} \text{ yr}^{-1}$  (for further discussion of the value for Ly $\alpha$  emitters, see [Matthee et al. 2017](#); [Verhamme et al. 2017](#)).

The second method calculates an unobscured SFR using the far-UV (FUV) continuum. We used the method of [Hao et al. \(2011\)](#), assuming a Kroupa IMF, solar metallicity, and 100 Myr age. We estimated the dust attenuation by measuring a NUV flux from the *HST*/ACS image and the FUV flux from the KCWI datacube. From this, we obtain  $\text{SFR}_{\text{FUV}} = 37.8 \text{ M}_{\odot} \text{ yr}^{-1}$ . Because of the uncertainty in the escape fraction of LyC photons, we adopt this SFR for the galaxy. Furthermore, the galaxy disk is parallel to our line-of-sight where dust blocks much of the light, which likely means that both the Ly $\alpha$  and the FUV luminosities are underestimated even despite the dust correction. This is corroborated in the SIMBA simulations, where the average  $z \sim 2$  star-forming galaxy with an absolute *B*-band magnitude comparable to the J1430+014,  $z_{\text{gal}} = 2.0711$  galaxy has  $\text{SFR} \sim 85 \text{ M}_{\odot} \text{ yr}^{-1}$ . The SFR measured here is most likely a lower limit.

From further examination of the *HST* image (left panel of Figure 1), it appears possible that this galaxy is located in a group environment with three galaxies just  $\sim 1''.8$  southward, particularly the galaxy that is bright in the KCWI whitelight image. Figure 4 explores the full spectra of both the identified host galaxy (top panels) and the bright continuum galaxy (bottom panels). The spectra are summed over eight spaxels indicated by the white boxes on the KCWI image zoom-ins (left) and are smoothed using a boxcar filter over eight voxels (spectral pixels). The spaxels are chosen to select a majority of the light from each galaxy but still be separated from each other enough to reduce potential cross-contamination due to the seeing and large Ly $\alpha$  halos. If we assume that both galaxies are located at  $z_{\text{gal}} = 2.0711$  and both contribute to the observed Ly $\alpha$  emission, then we can overlay the template spectrum for a Lyman break galaxy (LBG) from [Shapley et al. \(2003\)](#). This method for determining galaxy redshifts in low resolution data is often used for high-redshift objects (e.g., [Cooke et al. 2005, 2006](#)). The CGM host galaxy (top) matches the LBG template spectrum continuum level. Strong ISM absorption features such as OI, CII, SiII, SiIV, and CIV, and the SiII\* ISM emission lines appear to be present, though the spectrum is noisy. These all indicate that the measured redshift is likely real. In contrast, the continuum galaxy (bottom) does not match the continuum level across the wavelength range, with the lower flux at higher wavelength indicating that this is likely a lower redshift object. Nor does the continuum galaxy have the ISM features present, particularly CIV

absorption. This is true for all three galaxies south of the host galaxy in the *HST* image. We therefore conclude that the host galaxy has a large Ly $\alpha$  halo (either physically or due to the seeing) out to roughly  $1''.8$  and that it is likely isolated to the limits of our data. We assume the galaxy is isolated for the rest of our analysis.

### 3.2. Absorption System

From the VLT/UVES quasar spectrum, we identified several absorption lines associated with this host galaxy. The absorption system is plotted in Figure 5, where the UVES data and uncertainties are plotted as the black and green lines, respectively. While the quasar spectrum covers Ly $\alpha$ , which is important for metallicity analyses, neither the UVES nor KCWI spectra cover the rest of the Lyman series lines. Typical CGM metal lines such as MgII, CII, SiII, SiIII, SiIV, and CIV are detected and we further have coverage of, but no detected absorption for, MgI, OI, MnII, NII, FeII, and NV. Each detected unsaturated line has similar kinematics, with weaker components on either side of the bulk of the absorption near  $z_{\text{gal}}$ , but the ionization structure varies across the profile where the blueshifted weaker components are relatively stronger in SiIII and SiIV compared to SiII. These line-of-sight structure variations are further discussed in Section 4.3, but for comparison to the majority of the CGM metallicity literature, we focus on a total metallicity, which averages out the structure variations. As stated in Section 2.1, we model all absorption using VPFIT and describe our preferred fitting philosophy here.

We first fit the metal lines, where we took the approach of fitting the minimum number of VP components to obtain a reasonable chi-squared value (see e.g., [Churchill et al. 2003, 2020](#); [Evans 2011](#)). We assumed that doublets and multiplets for a given ion have the same kinematic structure (i.e., the MgII  $\lambda\lambda 2796, 2803$  doublet), but we did not require similar kinematic structure across ions (i.e., MgII compared to SiII or CII). The approach requiring similar kinematic structure across ions has been applied by the KBSS for understanding the thermal state of the  $z = 2 - 3$  CGM ([Rudie et al. 2019](#)), but we focus instead on obtaining the most accurate total column density for each ion.

Due to the fact that Ly $\alpha$  is saturated and the rest of the Lyman series lines are not covered in the spectrum, we constrained the HI column density using a combination of two methods (also see [Pointon et al. 2019](#)). We first fit a single VP component to Ly $\alpha$  and adopted this value as an upper limit. The lack of damping wings on the profile indicates that this absorber is not a DLA or sub-DLA and the best-fitting column den-

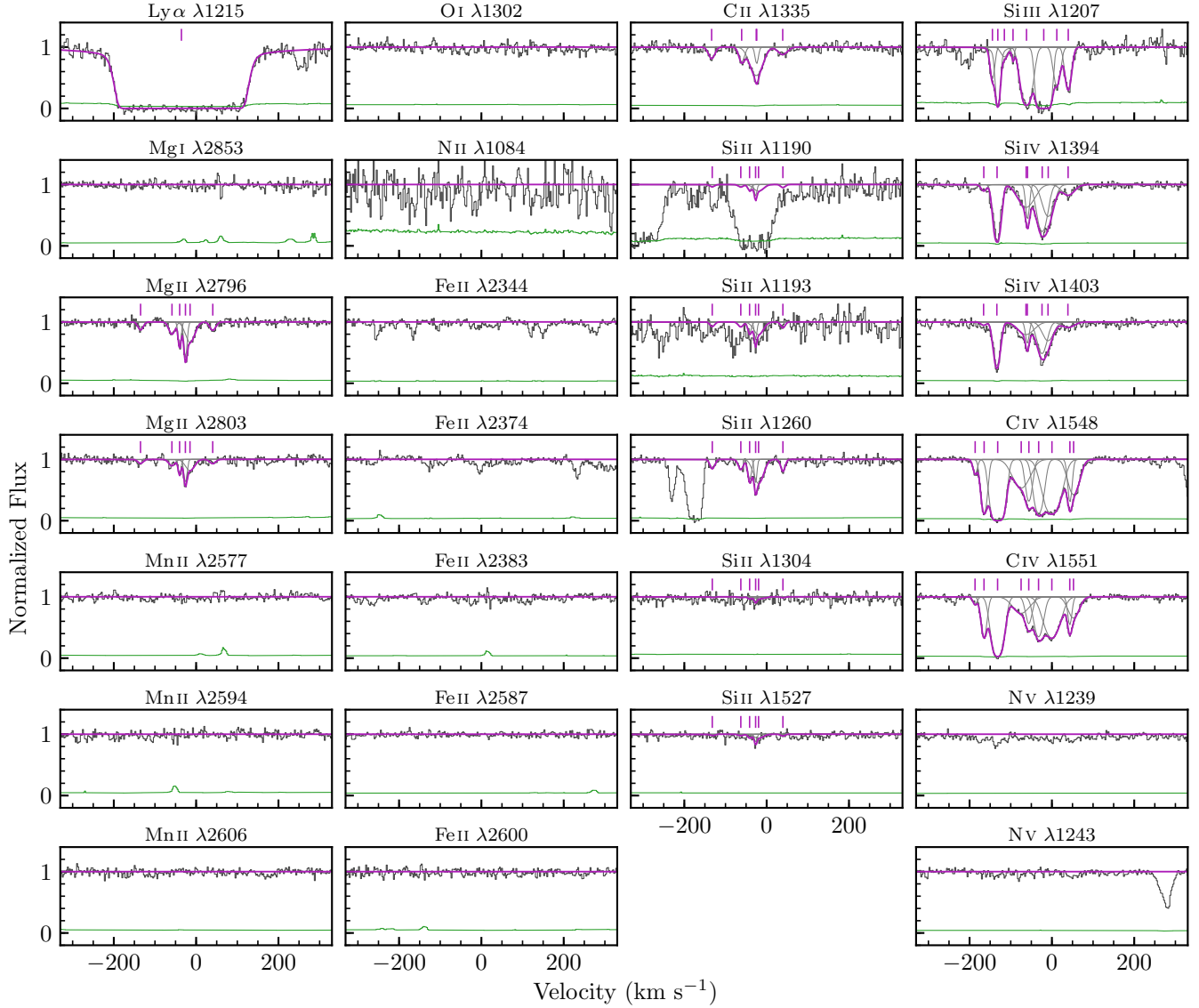


**Figure 5.** Absorption system at  $z_{\text{abs}} = 2.070789$  in the VLT/UVES spectrum of J143040+014939 covering the ions used in the metallicity analysis. The data for the ion transitions labeled above each panel are plotted as black histograms and the error spectra are the green histograms. The velocity zero point is  $z_{\text{gal}} = 2.0711$ . Voigt profile fits are plotted as purple lines while the purple ticks and gray lines indicate the individual Voigt profile components. Transitions in which only an upper limit on absorption could be measured have a purple horizontal line plotted through the data with no associated tick marks. With the exception of  $\text{Ly}\alpha$ , the strongest absorption is found in higher ions such as Si III, Si IV, and C IV.

sity,  $\log N_{\text{H I}} = 18.18 \text{ cm}^{-2}$ , indicates that this is most likely a LLS. We employed a second method where we applied the fit to  $\text{Mg II}$  as a template and fixed the VP component redshifts. The absorption system was then assumed to be dominated by thermal broadening, such that the ratio between the Doppler  $b$  parameters of  $\text{Ly}\alpha$  and  $\text{Mg II}$  for a given VP component is defined by the ratio between the atomic masses. This resulted in a value of  $\log N_{\text{H I}} = 16.37 \text{ cm}^{-2}$ . The H I column density is likely between the measurements with these two methods, but it is difficult to determine confidently due to the lack of

additional Lyman series lines. To be conservative in our H I column density range, we therefore adopted a lower limit of  $\log N_{\text{H I}} = 15.00 \text{ cm}^{-2}$ .

The results of our VP fitting are shown in Figure 5. The purple line demonstrates the VP model to the data, where individual VP components are plotted as gray curves and their velocity centroids are purple ticks. The plotted  $\text{Ly}\alpha$  fit is derived from the single component fit described above. Where absorption was not formally detected, we plot a horizontal purple line with no VP components. The velocity zero point is  $z_{\text{gal}}$ , which is

**Table 2.** Rest Absorption Equivalent Widths

Transition	EW (Å)	$v_-^a$ (km s $^{-1}$ )	$v_+^a$ (km s $^{-1}$ )
Ly $\alpha$ $\lambda$ 1215	$1.472 \pm 0.013$	-514	+381
MgI $\lambda$ 2853	$< 0.019$	...	...
OI $\lambda$ 1302	$< 0.009$	...	...
MgII $\lambda$ 2796	$0.241 \pm 0.010$	-151	+56
MgII $\lambda$ 2803	$0.137 \pm 0.010$	-147	+52
MnII $\lambda$ 2577	$< 0.010$	...	...
MnII $\lambda$ 2594	$< 0.011$	...	...
MnII $\lambda$ 2606	$< 0.011$	...	...
FeII $\lambda$ 2344	$< 0.008$	...	...
FeII $\lambda$ 2374	$< 0.009$	...	...
FeII $\lambda$ 2383	$< 0.008$	...	...
FeII $\lambda$ 2587	$< 0.009$	...	...
FeII $\lambda$ 2600	$< 0.011$	...	...
SiII $\lambda$ 1190	$0.029 \pm 0.009$	-144	+46
SiII $\lambda$ 1193	$0.053 \pm 0.010$	-144	+48
SiII $\lambda$ 1260	$0.104 \pm 0.004$	-147	+50
SiII $\lambda$ 1304	$0.011 \pm 0.006$	-137	+43
SiII $\lambda$ 1527	$0.023 \pm 0.005$	-140	+47
CII $\lambda$ 1335	$0.136 \pm 0.005$	-153	+62
NII $\lambda$ 1084	$< 0.034$	...	...
SiIII $\lambda$ 1207	$0.534 \pm 0.010$	-175	+60
SiIV $\lambda$ 1394	$0.405 \pm 0.005$	-181	+74
SiIV $\lambda$ 1403	$0.261 \pm 0.005$	-179	+69
CIV $\lambda$ 1548	$0.957 \pm 0.004$	-200	+89
CIV $\lambda$ 1551	$0.692 \pm 0.004$	-199	+86
NV $\lambda$ 1239	$< 0.005$	...	...
NV $\lambda$ 1243	$< 0.006$	...	...

<sup>a</sup>Velocity boundaries on absorption, defined as the velocity at which the VP model recovers to within 1% of the continuum. The values are relative to  $z_{\text{gal}} = 2.0711$ . To compare to  $z_{\text{abs}}$ , which is defined as the optical depth-weighted median of the MgII  $\lambda$ 2796 line, the conversion is  $v_{\text{abs}} = v_{(+/-)} + 27 \text{ km s}^{-1}$ .

redshifted from the optical depth-weighted median of absorption for the MgII  $\lambda$ 2796 line,  $z_{\text{abs}}$ , by  $27 \text{ km s}^{-1}$ .

Equivalent widths and velocity bounds relative to  $z_{\text{gal}}$  for each transition are tabulated in Table 2. These values were measured from the VP models instead of the data due to unrelated absorption in the data for several transitions (i.e., SiII  $\lambda$ 1190,  $\lambda$ 1193,  $\lambda$ 1260). Equivalent width upper limits are reported at the  $3\sigma$  level and were calculated using the observed spectrum to account for noise. The boundaries on absorption are de-

**Table 3.** Measured Column Densities

Ion	$\log N \text{ (cm}^{-2}\text{)}$
HI <sup>a</sup>	[15.00, 18.18]
MgI	$< 11.18$
OI	$< 13.13$
MgII	$12.88 \pm 0.02$
MnII	$< 11.70$
FeII	$< 11.74$
SiII	$12.95 \pm 0.03$
CII	$13.92 \pm 0.01$
NII	$< 13.62$
SiIII	$14.85 \pm 0.63$
SiIV	$13.91 \pm 0.01$
CIV	$14.79 \pm 0.01$
NV	$< 12.41$

<sup>a</sup>Ly $\alpha$  is saturated and no other Lyman series lines are covered, so we defined boundaries on this value. See Section 3.2 for details.

finer as the velocity at which the VP model recovers to within 1% of the continuum. It is interesting to note that the MgII equivalent width is consistent with the  $z < 1 W_r(2796) - D$  anti-correlation and log-linear fit from Nielsen et al. (2013a,b). A larger sample of  $z = 2$  absorber-galaxy pairs will investigate whether the relation evolves with redshift, where Chen (2012) did not find any evolution.

The measured column densities for each ion are listed in Table 3. The table lists two values for HI, which are the boundary values adopted from the fitting method described above. Column density upper limits were calculated using the  $3\sigma$  equivalent width upper limits and assuming a Doppler parameter of  $b = 8 \text{ km s}^{-1}$ , which is the typical value for SiII in the Pointon et al. (2019) sample. The choice of Doppler parameter does not change the measured value.

The kinematic structure of the metal lines is reminiscent of the structure found in the Milky Way Fermi bubbles (Fox et al. 2015; Bordoloi et al. 2017), where there is strong absorption near the systemic galaxy velocity and several higher velocity components that are roughly symmetrically redshifted and blueshifted. Recall that the host galaxy is assumed to be an edge-on galaxy probed along its minor axis, which is similar to the Milky Way and Fermi bubble geometry. Alternatively, the host galaxy could instead be a major merger, with the projected major axis of the merger aligned per-

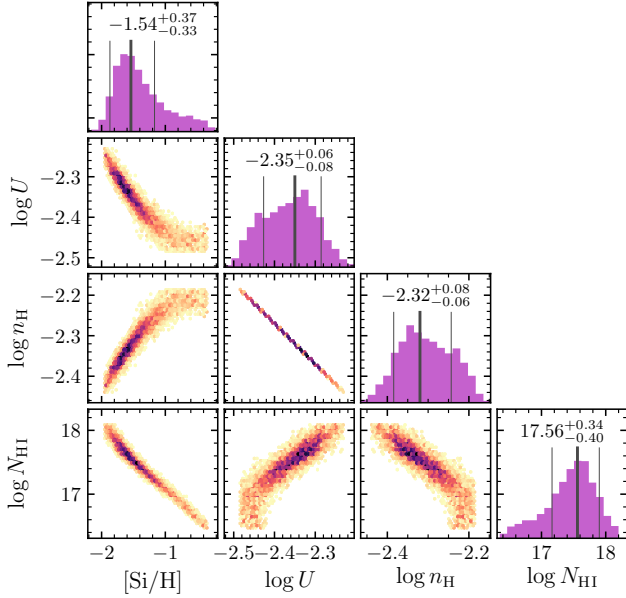


**Figure 6.** Posterior distributions from the MCMC modeling for metallicity,  $[\text{Si}/\text{H}]$ , ionization parameter,  $\log U$ , hydrogen density,  $\log n_{\text{H}}$ , and H I column density,  $\log N_{\text{HI}}$  for the All Ions run with HM05. Histograms show the sample distribution for each quantity, where the thin vertical lines indicate the smallest interval containing 68% of the MCMC samples and the thick vertical lines indicate the maximum likelihood value. We adopt a metallicity of  $[\text{Si}/\text{H}] = -1.5^{+0.4}_{-0.3}$ .

pendicular to the quasar sightline. Rupke et al. (2019) found bipolar outflow bubbles with an hourglass shape that are consistent with the structure of the Milky Way Fermi Bubbles in emission out to 50 kpc in a merger system (see also Burchett et al. 2020). Within this structure they found evidence for two outflow episodes that took place 0.4 Gyr ago and 7 Gyr ago. Given that the impact parameter of the system we study here at 66 kpc is not much further than the Rupke et al. system, the quasar sightline is perpendicular to the projected major axis of the galaxy, the absorption roughly symmetrically spans the galaxy redshift, and the galaxy is star-forming, it is possible that the quasar sightline is probing an outflowing cone of gas, with physical edges defined by the velocity edges of the absorption (see Table 2) regardless of the galaxy morphology. We further explore the observed kinematics with an outflow model in Section 3.5 and other scenarios that might describe the absorption properties in Section 4.4.

### 3.3. CGM Metallicity

In order to infer a total line-of-sight CGM metallicity for this absorber, we compared the observed column densities listed in Table 3 to the predicted column densities generated by CLOUDY with the HM05 UV back-

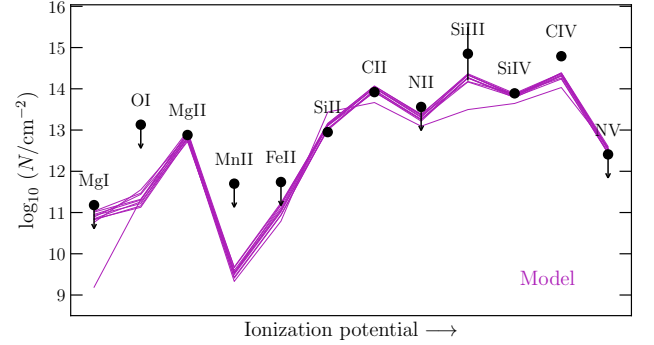


**Figure 7.** Comparison between the observed column densities (black points) and the predicted CLOUDY column densities for ten random MCMC samples (purple) for the All Ions run with HM05.

ground using an MCMC analysis and Bayesian statistics (for further details, see Section 2.1 and Pointon et al. 2019, 2020; Crighton et al. 2015, 2016 as well as Cooper et al. 2015; Fumagalli et al. 2016; Wotta et al. 2016, 2019; Prochaska et al. 2017; Lehner et al. 2019). The input CLOUDY grids span ranges of  $-5.0 < \log n_{\text{H}} < -2.0 \text{ cm}^{-3}$ ,  $13.0 < \log N_{\text{HI}} < 19.5 \text{ cm}^{-2}$ , and  $-3.0 < [\text{Si}/\text{H}] < 1.0$  with step sizes of 0.5 and are used as flat priors in the MCMC analysis. After testing, a minimum value of  $\log n_{\text{H}} > -3.1$  was enforced to avoid MCMC walkers getting stuck in local maxima (locally higher likelihood or probability). Nearly all LLSs studied in Lehner et al. (2016) were modeled to have hydrogen densities above this minimum value, so this lower limit is reasonable. Priors on the measured column density for each metal line are assumed to be a Gaussian distribution defined by the measured column density and its uncertainties as listed in Table 3. In the case that only an upper limit could be measured, these values were applied as one-sided Gaussian priors with a sigma of 5. For H I, the bounds on  $\log N_{\text{HI}}$  were applied as bounds on a flat prior, which allows the MCMC analysis to find a best-fit solution anywhere in that range. We assume a single-phase model in which column density measurements and upper limits for all ions listed in Table 3 were used. We explore how removing the highest ionization lines affects the inferred total metallicity of the low ionization gas below and additionally report the inferred values using the HM12 UV background for completeness in Table 4.

To avoid unphysically large cloud sizes, we restrict total cloud sizes to be below 100 kpc and apply this as a flat prior. While this upper limit allows for small sizes, applying a total cloud size upper limit of  $\sim 10$  kpc or below as a prior is too restrictive for the absorber studied here, resulting in unphysically small total cloud sizes of



**Table 4.** Inferred CGM Metallicities from Photoionization Modeling

Run	[Si/H]	$\log U$	$\log n_{\text{H}}$ ( $\text{cm}^{-3}$ )	$\log N_{\text{H I}}^a$ ( $\text{cm}^{-2}$ )	$\log N_{\text{H}}$ ( $\text{cm}^{-2}$ )
HM05 UV Background					
All Ions	$-1.5^{+0.4}_{-0.3}$	$-2.35^{+0.06}_{-0.08}$	$-2.32^{+0.08}_{-0.06}$	$17.6^{+0.3}_{-0.4}$	$20.5^{+0.3}_{-0.3}$
No N v	$-1.8^{+0.5}_{-0.1}$	$-2.14^{+0.01}_{-0.11}$	$-2.53^{+0.11}_{-0.01}$	$17.79^{+0.04}_{-0.55}$	$20.8^{+0.2}_{-0.2}$
No N v, C IV	$-1.7^{+0.7}_{-0.2}$	$-2.25^{+0.06}_{-0.18}$	$-2.42^{+0.18}_{-0.06}$	$17.7^{+0.1}_{-0.7}$	$20.5^{+0.4}_{-0.4}$
No N v, C IV, Si IV	$-1.6^{+0.4}_{-0.4}$	$-2.5^{+0.2}_{-0.2}$	$-2.2^{+0.2}_{-0.2}$	$17.6^{+0.5}_{-0.5}$	$20.5^{+0.4}_{-0.4}$
HM12 UV Background					
All Ions	$-0.43^{+0.07}_{-0.75}$	$-2.64^{+0.05}_{-0.02}$	$-2.25^{+0.02}_{-0.05}$	$16.67^{+0.65}_{-0.09}$	$19.8^{+0.5}_{-0.5}$
No N v	$-1.66^{+0.23}_{-0.02}$	$-2.234^{+0.001}_{-0.08}$	$-2.656^{+0.08}_{-0.001}$	$17.65^{+0.04}_{-0.23}$	$20.9^{+0.1}_{-0.1}$
No N v, C IV	$-1.80^{+0.29}_{-0.07}$	$-2.27^{+0.01}_{-0.13}$	$-2.62^{+0.13}_{-0.01}$	$17.84^{+0.08}_{-0.34}$	$21.0^{+0.1}_{-0.1}$
No N v, C IV, Si IV	$-1.84^{+0.36}_{-0.12}$	$-2.38^{+0.08}_{-0.29}$	$-2.51^{+0.29}_{-0.08}$	$17.92^{+0.14}_{-0.42}$	$20.8^{+0.3}_{-0.3}$

<sup>a</sup>These values are inferred from the MCMC analysis, but the value was assumed to be in the range of  $15.00 \leq \log N_{\text{H I}} \leq 18.18$  from Table 3.

$\sim 10$  pc or MCMC walkers getting stuck in their initial positions. This *total* cloud size value of  $\sim 10$  pc is over an order of magnitude smaller than the *component* cloud sizes estimated by Crighton et al. (2015), who found component cloud sizes to range from 100 – 500 pc. This corresponds to a total cloud size of 600 – 3000 pc for a six component absorber (i.e., Mg II) or 900 – 4500 pc for a nine component absorber (i.e., C IV). A total cloud size of 10 pc is also over an order of magnitude smaller than the total cloud sizes inferred by Lehner et al. (2016), who studied a statistical sample of  $z \sim 2$  LLSs and pLLSs, where their total cloud sizes range from 0.07 – 1862 kpc (mean of 112 kpc and median of 14 kpc).

Figure 6 presents the posterior distributions from the MCMC modeling for metallicity, [Si/H], ionization parameter,  $\log U$ , hydrogen density,  $\log n_{\text{H}}$ , and H I column density,  $\log N_{\text{H I}}$  for the All Ions run using the HM05 UV background. For the analysis, 100 walkers were initialized with a burn-in stage of 200 steps and then were run for another 200 steps to determine the final distributions. Histograms show the distributions for each quantity, where the vertical lines indicate the maximum likelihood value (thick lines) with 68% confidence interval uncertainties (thin lines). The final adopted values for metallicity, ionization parameter, hydrogen density, H I column density, and total hydrogen column density are listed in Table 4. Our analysis infers a metallicity of  $[\text{Si}/\text{H}] = -1.5^{+0.4}_{-0.3}$  when all ions are included.

A comparison between the measured column densities and ten random MCMC sample predictions is plotted in Figure 7 for the All Ions run with HM05. Black points represent the column densities from Table 3, where the uncertainties on the points are mostly smaller than the points themselves. The large uncertainty on the Si III line is due to saturation at  $v = 0$  km s $^{-1}$ . The purple lines indicate the ten MCMC samples, which reasonably predict most column densities. However, the models do not accurately predict C IV, which is likely due to the fact that the ion traces intermediate ionization gas. C IV often displays kinematics that are consistent with both the low ions (e.g., Mg II and Si II) and the high ions (e.g., O VI). While we do not have coverage of O VI for this absorption system here to further examine this, the intermediate ionization kinematic behavior is discussed in, e.g., Rudie et al. (2019).

Another potential reason for the discrepancy between the measured C IV column density and the model values is that we include N v in the analysis, which is a higher ionization transition. In this case, our assumption of a single phase may break down. To investigate the dependence of metallicity on the inclusion of the higher ions, we conduct a test removing N v, C IV, and Si IV from the MCMC analysis one-by-one. The results of these tests are listed in Table 4 for comparison. Overall the resulting metallicities are all consistent within uncertainties, even between the “all ions” and “no N v” runs, which

represent the extremes in metallicity. We examined the comparison between the observed column densities and predicted CLOUDY column densities (i.e., Figure 7) for the “no NV” run and found that the models more accurately predict the CIV column densities, but the comparison for the rest of the ions does not differ appreciably. For the “no NV, CIV” and “no NV, CIV, SiIV” runs, the random models continue to trace the observed (included) ions similarly to those plotted in Figure 7, but the variation in the models increases. This latter comparison suggests that CIV and SiIV provide important constraints on the metallicity estimate, which is sensible since these ions exhibit kinematic structures that are similar to the lower ions. The assumption of a single phase may then be valid in this system. We cannot investigate this further since it requires partitioning HI between phases, which is difficult with only the saturated Ly $\alpha$  line and we do not wish to over-interpret the system. The total cloud sizes (cloud size =  $N_{\text{H}}/n_{\text{H}}$ ) derived from this modeling and single phase assumption are reasonable, with 21 kpc for the All Ions run, 69 kpc for “no NV”, 27 kpc for “no NV, CIV”, and 16 kpc for “no NV, CIV, SiIV”. These values are consistent with the  $z = 2$  LLSs studied by Lehner et al. (2016). Given the results of these tests, we adopt the metallicity inferred from the “all ions” run with HM05 for the remainder of our analysis.

For comparison to other work that uses the HM12 UV background, we also modeled the absorption system after changing HM05 to HM12 but keeping the priors and CLOUDY grids the same. These results are listed in Table 4. There is a much larger variation in the metallicity inferred between the four different runs, with the All Ions run having a higher metallicity than the other runs and all HM05 runs. It appears that the inclusion of NV with HM12 skews the metallicity toward much higher values because the values decrease once NV is removed from the analysis. This would not be unexpected since a multiphase and multicomponent analysis of a  $z = 0.4$  absorber–galaxy pair found a higher metallicity for the higher ionization phase (e.g., Muzahid et al. 2015). The downward uncertainties on this HM12 All Ions run are clearly large, indicating that the metallicity is likely lower, and are consistent with the All Ions run with HM05. Other than the All Ions run, the HM12 results are all consistent within uncertainties and consistent with their comparable HM05 runs. The choice of UV background does not significantly affect our conclusions.

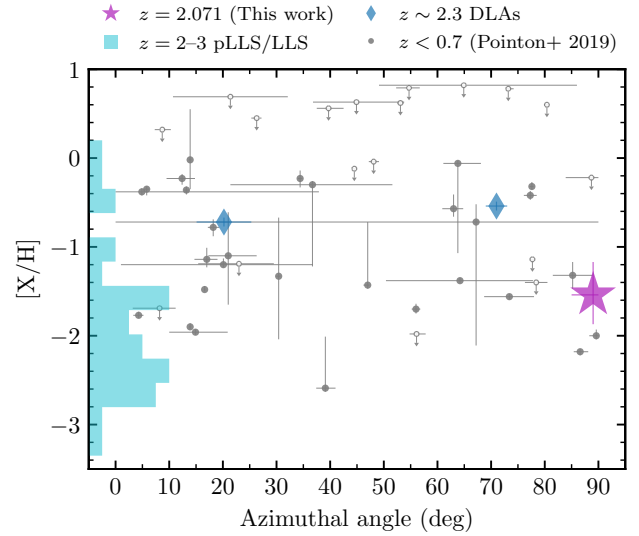


**Figure 8.** CGM metallicity,  $[X/H]$ , as a function of azimuthal angle,  $\Phi$ . Galaxies probed along their projected major axis have  $\Phi = 0^\circ$ , while galaxies probed along their projected minor axis have  $\Phi = 90^\circ$ . The J1430+014,  $z = 2.071$  minor axis absorber (this work) is plotted as the purple star, while the  $z \sim 2.3$  DLAs from Bouché et al. (2013) and Krogager et al. (2013) are plotted as the blue diamonds. The cyan histogram shows the distribution of pLLS/LLS at  $z = 2 - 3$  from Crighton et al. (2013, 2015) and Lehner et al. (2014, 2016). Also plotted for comparison are gray points, which represent CGM metallicities for isolated galaxies at  $z < 0.7$  from Pointon et al. (2019), where solid points indicate metallicity measurements and open points indicate upper limits on the CGM metallicity.

### 3.4. Metallicity–Azimuthal Angle Relation

At low redshift,  $z < 0.7$ , Pointon et al. (2019) found that the total CGM metallicity along the line-of-sight does not depend on the orientation at which the quasar probes isolated galaxies within 200 kpc. The authors suggested that the lack of a dependence may partially be due to studying the CGM during a time at which gas flows are diminishing in strength. Here we place the J1430 + 014,  $z = 2.071$  absorber–galaxy pair in the context of both this low redshift survey and  $z = 2 - 3$  metallicity distributions. Figure 8 presents the available data sets, which will later be used with our full program to understand if gas flows are more distinct on this plane when galaxies are most actively building up their stellar mass. The Pointon et al. (2019) data are plotted as gray points for comparison, where upper limits on the metallicity are plotted as open points. The metallicities for the Pointon et al. sample were measured with the same methods used here, so we can directly compare their values.

Since the absorber we study here is a pLLS or a LLS (see Table 3 for the adopted  $\log N_{\text{H I}}$  range), we plot a cyan histogram of the  $z = 2 - 3$  pLLS/LLS sample from Crighton et al. (2013, 2015) and Lehner et al. (2014, 2016) on the y-axis for comparison.<sup>2</sup> In most cases, host galaxies have not yet been identified for that sample and where they have been identified, there is no published morphology information. Also plotted are two  $z \sim 2.3$  DLAs (blue diamonds) with measured azimuthal angle information (Bouché et al. 2013; Krogager et al. 2013). The J1430+014,  $z = 2.071$  absorber studied here is plotted as the purple star. The figure is currently sparsely populated by  $z = 2 - 3$  absorber–galaxy pairs, but we aim to expand the sample with our KCWI program. Recall that the KBSS (Rudie et al. 2012) also examines the CGM over this redshift range, but does not currently provide the CGM metallicities nor azimuthal angles.

The J1430+014,  $z = 2.071$  absorber is consistent with the range of metallicities found at low redshift,  $z < 0.7$ , although it is on the lower end of the range. This is expected since the metallicity of pLLSs/LLSs evolves from lower metallicities at  $z = 2 - 3$  to higher metallicities at  $z < 1$  (Lehner et al. 2016). Compared to the  $z = 2 - 3$  pLLSs/LLSs, the J1430+014 absorber is slightly more metal-rich than the peak in the distribution at  $[X/H] \sim -2$ . Thus it is likely that the gas was previously in the galaxy at some point, where an outflow is a plausible source of the observed gas in this sightline. We expand on this further in Section 3.5, where we model the gas as an outflowing cone.

Thus far there are only three  $z = 2 - 3$  sightlines where both CGM metallicities and galaxy morphologies have been measured. Compared to the minor axis DLA at  $D = 6$  kpc from Krogager et al. (2013) and the major axis DLA at  $D = 26$  kpc from Bouché et al. (2013), our absorber–galaxy pair is more metal-poor. However, DLAs are known to be more metal-rich than pLLSs/LLSs since the background quasar is thought to probe the disks or near the disks of the host galaxies, so this result is not unexpected (e.g., Lehner et al. 2016). From these three points, it is unclear if the separation between metal-poor, major axis gas and metal-rich, minor axis gas will be clear at  $z = 2 - 3$ . Péroux et al. (2020) studied the CGM metallicity–azimuthal angle plane in the EAGLE and IllustrisTNG simulations

and suggested that there should not be a clear trend at this redshift due to galaxies not having enough time to adequately pollute their CGM with metal-enriched gas. In order to best examine this, we need a large sample of absorber–galaxy pairs with similar H I column density ranges (i.e., pLLSs/LLSs). We plan to further explore the CGM metallicity–galaxy relation with a larger sample of  $z = 2 - 3$  absorber–galaxy pairs in the future.

### 3.5. Outflow Modeling

Assuming the host galaxy has an edge-on morphology, the kinematics and metallicity of the observed gas and its location relative to the host galaxy suggest the gas is plausibly outflowing material. If we then assume outflowing material, we can use the combination of Mg II kinematics and galaxy geometry in the conical model detailed by Gauthier & Chen (2012) to constrain the outflow velocity and opening angle.<sup>3</sup> Figure 1 in their paper best illustrates the model, which we briefly describe here. The outflow is defined as an outwardly expanding polar cone emanating from the galaxy center with a full angular span of  $2\theta_0$ . The quasar sightline enters the outflowing cone at a height above the galaxy disk  $z_1$  and exits at  $z_2$ , both of which depend on the galaxy geometry and outflow opening angle, where we require that  $z_1 < z_2$ . The galaxy has an inclination,  $i$ , and azimuthal angle,  $\Phi$ , which is the angle between the projected galaxy disk and the background quasar sightline. The quasar is located at an impact parameter,  $D$ , from the galaxy. All galaxy properties are defined in Table 1 for the absorber–galaxy pair studied here.

The relation between the half opening angle,  $\theta_0$ , and  $z_{[1,2]}$ , which is the outflow disk (i.e., a slice through the outflow cone parallel to the galaxy) at heights  $z_1$  and  $z_2$ , is

$$z_{[1,2]} \tan \theta_0 = D \sqrt{1 + \sin^2 \phi_{[1,2]} \tan^2 i} \left( \frac{\cos \Phi}{\cos \phi_{[1,2]}} \right). \quad (1)$$

The position angle between the quasar sightline and the outflow disks projected on the sky,  $\phi_{[1,2]}$ , is defined by

$$\tan \phi_{[1,2]} = \frac{D \sin \alpha - z_{[1,2]} \sin i}{D \cos \alpha}. \quad (2)$$

<sup>2</sup> Also see Fumagalli et al. (2016). Note that the authors of that study use the HM12 ionization background. At low redshifts, HM12 results in metallicities that are roughly 0.3 dex higher than the HM05 background we use here. Table 4 lists HM12 results for comparison to Fumagalli et al. (2016) but we refrain from doing the comparison here as our focus is on the large body of work at low redshift, which mostly uses HM05.

<sup>3</sup> While the Gauthier & Chen (2012) model can explain the observed velocity space in the absorption profiles, it does result in velocity gradients that are too large compared to momentum-driven outflow models (e.g., supernovae feedback). However, this simple model results in outflow characteristics that are comparable to the simple outflow models of Bouché et al. (2012), Martin et al. (2019), and Schroetter et al. (2016, 2019), so we use the model here for comparison to other work.

Using Equations 1 and 2 we can then calculate the angle,  $\theta$ , along the quasar sightline for a height  $z$ , where  $z_1 \leq z \leq z_2$ . Finally, the outflow speed,  $V_{\text{out}}$ , of a gas cloud moving outward from the galaxy at height  $z$  is related to the line-of-sight velocity,  $v_{\text{los}}$ , and  $\theta$  with

$$V_{\text{out}} = \frac{v_{\text{los}}}{\cos j}, \text{ where } j = \sin^{-1} \left( \frac{D}{z} \cos \theta \right), \quad (3)$$

and  $\theta \leq \theta_0$ .  $V_{\text{out}}$  is the radial outflow speed from the galaxy, which varies with  $z$ -height above the galaxy, and depends on the line-of-sight velocity and the half opening angle of the outflow cone for a given  $z$ -height. This value is not necessarily constant.

From all of this, the input values for the model include absorption velocity bounds  $v_{\text{los},1}$  and  $v_{\text{los},2}$ , galaxy properties  $D$ ,  $i$ , and  $\Phi$ , and the range of possible  $z$ -heights from 0 kpc to 1000 kpc. The model assumes that the MgII-absorbing gas fills the outflow cone such that the velocity bounds on absorption represent the physical bounds on the cone. These bounds are  $v_{\text{los},1} = 56 \text{ km s}^{-1}$  and  $v_{\text{los},2} = -151 \text{ km s}^{-1}$  and were determined by identifying the velocities relative to  $z_{\text{gal}}$  at which the absorption profile recovers to within 1% of the continuum (see Table 2 and Section 3.2). The line-of-sight velocities are assumed to increase smoothly as the quasar sightline passes through the outflow cone towards larger  $z$ -heights, which implies that the outflow cone is pointed towards the observer rather than away.

Figure 9 presents the allowed  $z$ -heights, half opening angles, and outflow velocities for the J1430+014,  $z = 2.071$  absorber–galaxy pair, assuming the host galaxy is a single object with an edge-on inclination. The purple dashed line represents the location at which the quasar sightline enters the outflowing cone, while the solid cyan line is the exit location. The model requires that  $z_1 < z_2$ , which is true in the upper panel for all half opening angles. From the lower panel, the outflow velocity decreases from  $z_1$  to  $z_2$  for all half opening angles, indicating that the gas is decelerating as it outflows. With these curves, we can then constrain the allowed half opening angle,  $\theta_0$ , and therefore the outflow velocity,  $V_{\text{out}}$ . Considering only the absorber–galaxy geometry, the minimum half opening angle allowed depends on the azimuthal angle between the projected galaxy disk and the quasar sightline,  $\Phi = 89^\circ$ . In order for the sightline to pass through MgII-absorbing gas, the half opening angle must be at least the difference  $\theta_0 = 90^\circ - \Phi = 1^\circ$  (recall that  $\Phi = 90^\circ$  is defined as the projected galaxy minor axis, which defines  $\theta_0 = 0^\circ$  for an edge-on galaxy). Because the MgII absorption spans the galaxy systemic velocity, i.e., the gas is both redshifted and blueshifted, we cannot constrain

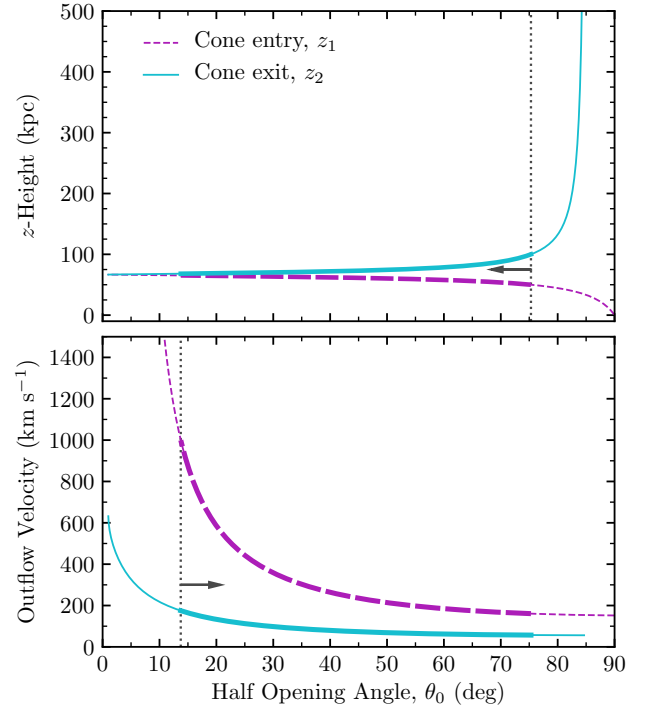


**Figure 9.** Outputs from modeling the MgII absorption as a polar outflowing cone:  $z$ -heights, half opening angles, and outflow velocities. The quasar sightline enters the outflowing cone at  $z_1$  (dashed purple) and exits the cone at  $z_2$  (cyan), where  $z_1 < z_2$ . Vertical dashed lines and thicker curves indicate allowed half opening angles, beyond which the  $z$ -heights or outflow velocities asymptote to unrealistically large values. The gas is decelerating for all half opening angles.

the maximum opening angle allowed based on geometry alone.

Further considering the distributions of the model parameters in Figure 9, we find that the  $z$ -heights asymptote beyond  $\theta_0 \sim 80^\circ$ . At these large  $\theta_0$  values, the quasar sightline does not exit the cone beyond  $\theta_0 \simeq 85^\circ$  because the opening angle is large enough for the edge of the cone to be parallel to the quasar sightline. Given this, we imposed a maximum allowed  $z$ -height of 100 kpc, which was chosen to roughly correspond to the virial radius of a  $\log(M_{\text{h}}/M_\odot) = 12.0$  galaxy at this redshift. The vertical dashed line in the upper panel indicates the half opening angle corresponding to this limit,  $\theta_0 = 75^\circ$ . Similarly, the lower panel shows that the outflow velocities asymptote to large values below  $\theta_0 \sim 10^\circ$ , which is unrealistic since outflows are generally found to be collimated and have velocities on the order of several hundred  $\text{km s}^{-1}$  (e.g., Bordoloi et al. 2011, 2014b; Bouché et al. 2012; Kacprzak et al. 2014; Lan et al. 2014;



Rubin et al. 2014; Schroetter et al. 2016, 2019).<sup>4</sup> Using stacked galaxy spectra, Steidel et al. (2010) suggested that outflows at  $z = 2$  have velocities on the order of  $V_{\text{out}} \simeq 800 \text{ km s}^{-1}$ . We therefore constrain the lower opening angle value using a maximum outflow velocity of  $1000 \text{ km s}^{-1}$  and this is indicated by the vertical dotted line in the bottom panel of Figure 9.

The allowed values from the model are then  $14^\circ \leq \theta_0 \leq 75^\circ$  and are further indicated as the thick curves in Figure 9. The average outflow velocities corresponding to these opening angles (i.e., the average between the purple and cyan curves) are  $V_{\text{out}} \sim 588 \text{ km s}^{-1}$  for  $\theta_0 = 14^\circ$  down to  $V_{\text{out}} \sim 109 \text{ km s}^{-1}$  for  $\theta_0 = 75^\circ$ . The velocities could be as large as  $1000 \text{ km s}^{-1}$  or as small as  $57 \text{ km s}^{-1}$ . Unfortunately these cannot be constrained further with the geometry of the system. If we account for the uncertainty in the galaxy redshift that results from the apparent redshift of the Ly $\alpha$  emission,  $\pm 78 \text{ km s}^{-1}$ , we find slight changes to the model results. When a larger Ly $\alpha$  correction is applied, the absorption still spans the galaxy systemic redshift, the outflow half opening angles could be as small as  $9^\circ$ , and the gas may accelerate slightly as it moves further from the galaxy, but the velocities do not change significantly. If a smaller Ly $\alpha$  correction is applied, the absorption then shifts to being completely blueshifted from the galaxy systemic redshift by  $-105 \text{ km s}^{-1}$  and the geometry of the system constrains the half opening angles to  $1^\circ \leq \theta_0 \leq 5^\circ$ . These opening angles are highly collimated in contrast to the simulations and other observations at this epoch and may be unlikely for a star-forming galaxy with no obvious AGN activity to the limits of the data.

### 3.6. Outflow Timescales, Mass Outflow Rates, & Mass Loading Factors

Having assumed an edge-on galaxy morphology and modeled the outflow velocities and half opening angles, we can characterize the impact of the outflows on the CGM. Although the models suggest the gas is decelerating, we assume a constant outflow velocity and estimate the time it takes for the observed gas to reach  $D = 66 \text{ kpc}$  from the galaxy. The values are tabulated in Table 5 for various outflow constraints. At the lower bound for the half opening angle, the outflow velocity is estimated to be  $V_{\text{out}} = 588 \pm 413 \text{ km s}^{-1}$ , which

<sup>4</sup> However, down-the-barrel observations by Law et al. (2012) suggest that  $z = 2$  outflows may not yet be collimated because the host galaxy disks are still unstable to rotation (also see Steidel et al. 2010), and this may also be true in simulations (e.g., Nelson et al. 2019). A larger sample is required to better investigate this.

**Table 5.** Outflow Modeling Results

$\theta_0^a$	$V_{\text{out}}$	$t_{\text{out}}^b$	$\dot{M}_{\text{out}}^c$	$\eta^c$
(deg)	( $\text{km s}^{-1}$ )	(Myr)	( $M_\odot \text{ yr}^{-1}$ )	
Maximum $V_{\text{out}}$				
14	1000	65	88	2.3
75	161	404	77	2.0
Average $V_{\text{out}}^d$				
14	588	111	51	1.4
75	109	597	52	1.4
Minimum $V_{\text{out}}$				
14	175	371	15	0.4
83	57	1140	27	0.7

<sup>a</sup>The lower bound is constrained with a maximum allowed  $V_{\text{out}}$  while the upper bound is constrained with a maximum allowed  $z$ -height (i.e., impact parameter).

<sup>b</sup>Timescale to  $D = 66 \text{ kpc}$  given a constant  $V_{\text{out}}$ .

<sup>c</sup>The values reported in these column are considered upper limits due to the uncertainty in the outflow and metallicity modeling.

<sup>d</sup>Values calculated using the mean  $V_{\text{out}}$  between the  $z_{[1,2]}$  curves at the given  $\theta_0$ .

results in an outflow timescale of  $t_{\text{out}} \sim 111^{+260}_{-46} \text{ Myr}$  or an ejection redshift of  $z_{\text{eject}} \sim 2.15$ . The maximum outflow timescale comes from the upper bound on the half opening angle, where  $V_{\text{out}} = 109 \pm 52 \text{ km s}^{-1}$ ,  $t_{\text{out}} \sim 597^{+543}_{-193} \text{ Myr}$ , and  $z_{\text{eject}} \sim 2.55$ . These timescales decrease if the gas is instead assumed to be decelerating as it moves outwards from the galaxy.

Despite the large range of allowed half opening angles and outflow velocities of the potential outflowing gas, we can also estimate mass outflow rates and mass loading factors to understand how much material the galaxy is being ejected into the CGM. From Bouché et al. (2012) and Schroetter et al. (2016, 2019), the mass outflow rate is roughly

$$\frac{\dot{M}_{\text{out}}}{0.5 M_\odot \text{ yr}^{-1}} \approx \frac{\mu}{1.5} \frac{N_{\text{H}}}{10^{19} \text{ cm}^{-2}} \frac{D}{25 \text{ kpc}} \frac{V_{\text{out}}}{200 \text{ km s}^{-1}} \frac{\theta_0}{30^\circ}, \quad (4)$$

where  $\mu$  is the mean atomic weight of 1.4. We estimated the total hydrogen column density,  $N_{\text{H}}$ , from the photoionization modeling in Section 3.3 for the “all ions” run, with  $\log N_{\text{H}} = 20.5 \text{ cm}^{-2}$ . Then the mass loading factor is

$$\eta = \frac{\dot{M}_{\text{out}}}{\text{SFR}}. \quad (5)$$

Table 5 details the mass outflow rates and mass loading factors for the various opening angle and outflow velocity constraints. The mass outflow rate is roughly  $\dot{M}_{\text{out}} \sim 52 \pm 37 \text{ M}_{\odot} \text{ yr}^{-1}$ , corresponding to mass loading factors of  $\eta \sim 1.4 \pm 1.0$ . These values are likely upper limits given the galaxy’s assumed edge-on inclination, the uncertainty in the total hydrogen column density from the metallicity modeling, the high likelihood that the outflow has swept up additional CGM material along the way, and that the values are the maximum values obtained if a larger or smaller  $\text{Ly}\alpha$  redshift correction defined by the uncertainty on the redshift is applied.

These mass outflow rates are roughly an order of magnitude larger than most values reported by the MEGAFLOW survey at  $z \sim 1$  (Schroetter et al. 2016, 2019). While this may be due to more energetic outflows at  $z \sim 2$  (see discussion in the next section), the measurement uncertainties are also important. In addition to the degeneracies in modeling the outflow half opening angles and velocities, there is a large uncertainty involved in measuring the total hydrogen column density. MEGAFLOW convert their  $\text{MgII}$  equivalent widths to  $N_{\text{H}}$ , using the Ménard & Chelouche (2009) relation and assume that the ionized gas contribution is negligible, such that  $N_{\text{H}} \approx N_{\text{H}}$ . Our  $N_{\text{H}}$  is inferred from the photoionization modeling and accounts for the possibility that hydrogen is also associated with gas that is higher ionization than  $\text{MgII}$ , such as  $\text{CIV}$  which is measured for our absorber. Compared to MEGAFLOW, our  $\text{MgII}$  absorber has a smaller equivalent width, but our total hydrogen column density is larger than most objects in their sample. This suggests that mass flow rates determined from statistical relations with large intrinsic scatter should be viewed with caution.

#### 4. DISCUSSION

As detailed in the previous sections, the combination of absorbing gas observed along the minor axis of an assumed edge-on galaxy with broad kinematics symmetrically distributed around  $z_{\text{gal}}$  suggests an outflow origin despite the large impact parameter, while the relatively metal-enriched metallicity suggests the outflow likely entrained lower metallicity gas on its way out from the galaxy. This is not unexpected since even at low redshift,  $z < 1$ , outflows appear to influence the CGM out

to at least 50 kpc (Bordoloi et al. 2011) and potentially further (100 kpc; Lan & Mo 2018; Schroetter et al. 2019). Outflows at  $z = 2$  are more energetic with higher velocities and mass loading factors (e.g., Sugahara et al. 2017). It could be expected that the material ejected from these outflows could reach larger galactocentric distances than measured at low redshifts, although the outflows would be competing with increased accretion rates as well. There is already potential evidence of outflowing material reaching out to 180 kpc at  $z = 2$  (Turner et al. 2014, 2015, 2017). These large impact parameters also result in long timescales and sufficiently early ejection redshifts for the SFR measured to be a lower limit.

##### 4.1. Galaxy Morphology

Our determination that the observed CGM gas has an outflow origin relies partially on the galaxy morphology, which can be difficult to quantify at  $z = 2$  due to the clumpy nature of galaxies at this epoch (e.g., Guo et al. 2015, and references therein). In a shallow *HST*/ACS image covering rest-frame UV wavelengths (F625W), we find two bright clumps with fainter material, but still a considerable amount of continuum, distributed in a rough plane perpendicular to the quasar sightline. These clumps likely correspond to separate star formation regions in the object given the wavelength coverage. This morphology is similar to both the “double” and “chain” galaxy morphologies studied in the *HST* Ultra Deep Field (e.g., Elmegreen et al. 2007). Galaxies with two clumps are common at this epoch (e.g., Shibuya et al. 2016) but the physical origin of these clumps is still debated in the literature. Shibuya et al. (2016) suggest that objects with this two-clump morphology are only formed via a violent disk instability whereas Ribeiro et al. (2017) suggests that they are formed via major mergers. Fisher et al. (2017) studied DYNAMO galaxies identified as low redshift analogs of star-forming galaxies at  $z = 1 - 3$ . The authors found that multiple clumps that are clustered in the disks of these galaxies appear as fewer, larger clumps in the lower resolution imaging that is common at higher redshift. This further complicates the interpretation of double clump morphologies, especially in shallow imaging.

As these works show, it is difficult to determine if two-clump morphologies are mergers or disk galaxies from morphological or kinematic classification alone (Shapiro et al. 2008; Hung et al. 2015). To best determine whether our object is a merger or not, we would require both morphology and kinematics (Rodrigues et al. 2017). We do not currently have kinematics for this object to better classify its morphology since the spaxels

on the medium slicer for KCWI have sizes on the order of the size of  $z \sim 2$  galaxies. Regardless, [Simons et al. \(2019\)](#) discussed that even with both photometry and kinematics, it may still be difficult to distinguish between a rotating disk and a merger at  $z \sim 2$ . This is because merging galaxies can have kinematic properties that match several criteria used to identify disks at high redshift (e.g., the five disk criteria comparing kinematic axes, velocity dispersions, and velocity gradients used by [Wisnioski et al. 2015](#)).

The separation of the two clumps in our object may be a distinguishing property to determine if the object is best modeled as a major merging system or a single clumpy galaxy. The two clumps are separated by only  $0''.23$ , corresponding to 1.9 kpc at this redshift. This separation is smaller than the typical half light radius of star-forming galaxies at  $z \sim 2$  ( $\sim 2.5 - 3$  kpc; [Allen et al. 2017](#)) and may indicate that the two clumps are part of a single object. [van der Wel et al. \(2014\)](#) studied the sizes of both star-forming and quiescent galaxies and found similar sizes as [Allen et al. \(2017\)](#) for star-forming galaxies, but smaller sizes for quiescent galaxies on the order of  $\sim 1$  kpc at  $z \sim 2$ . It is possible that the clumps in our object are two spheroids in the process of undergoing a major merger, but the object is star-forming and the spatial resolution of KCWI does not allow us to determine separate SFRs of the clumps. If this object is a merger, then we might reasonably assume that the star formation rate should be elevated relative to the star formation main sequence at this redshift. The unobscured SFR for this galaxy,  $\text{SFR}_{\text{FUV}} = 37.8 \text{ M}_{\odot} \text{ yr}^{-1}$ , is roughly on the main sequence for  $z \sim 2$  galaxies with stellar masses of  $\log(M_*/M_{\odot}) \sim 10$  (e.g., [Daddi et al. 2007](#); [Speagle et al. 2014](#)), so a merger seems less likely. While [Pearson et al. \(2019\)](#) suggest that a merger does not necessarily result in highly elevated star formation rates, they do find that the merger fraction increases the further a galaxy is away from the star formation main sequence. The main sequence SFR of our object indicates that a major merger morphology may have a lower probability than a single clumpy galaxy morphology.

Fortunately, simulations can provide some insight into this problem where observations currently struggle. [Simons et al. \(2019\)](#) studied theoretical merger fractions and the probability that mergers are classified as disks with the [Wisnioski et al. \(2015\)](#) disk criteria. The authors estimated that 5-15% of disks identified at these redshifts with kinematic criteria are actually mergers. More relevant to the work presented here is that [Simons et al. \(2019\)](#) found that the fraction of  $z \sim 2$  Illustris galaxies with a companion within a 2D projected separation of  $\sim 2$  kpc (i.e., the separation of the two clumps

in our object) is at most 2–3% for all merging systems,  $\sim 1\%$  for low mass major mergers, and nearly 0% for high mass major mergers. Given the low probability of merging galaxies with this separation, the separation of the two clumps being smaller than typical star-forming galaxies, and the low fraction of merging galaxies on the star formation main sequence (where this object lies at this redshift), we make the assumption that the object we observed is a single, clumpy, edge-on galaxy.

#### 4.2. Outflow Kinematics

Assuming the galaxy is a clumpy disk with an edge-on inclination from the discussion in the previous section, and having determined that the galaxy is star-forming with  $\text{SFR}_{\text{FUV}} = 37.8 \text{ M}_{\odot} \text{ yr}^{-1}$ , we modeled the observed gas as an outflow. The kinematics of the metal lines, where absorption is detected, all have similar velocity distributions and are all reminiscent of the profiles found in the Milky Way Fermi bubbles. That is, the gas is roughly centered on the galaxy systemic redshift,  $z_{\text{gal}}$ , for this edge-on galaxy and this is where the bulk of the absorption lies. There are additional roughly symmetric higher velocity components out to  $v \pm 50 - 150 \text{ km s}^{-1}$  for the lower ionization lines. Furthermore, the full velocity width of MgII,  $\Delta v \sim 210 \text{ km s}^{-1}$ , is consistent with the large velocity separation tail in the pixel-velocity two-point correlation function of the bluer (more highly star-forming) galaxies probed along their projected minor axes in [Nielsen et al. \(2015\)](#). The authors concluded these long tails were consistent with biconical outflows with large velocity dispersions. All of these corroborating inferences imply that the observed gas fills an outflowing cone, where absorption velocity bounds define the physical bounds on the cone. This commonly invoked scenario results in reasonable average outflow velocities ( $109 < V_{\text{out}} < 588 \text{ km s}^{-1}$ ) at half opening angles ( $14^\circ < \theta_0 < 75^\circ$ ) that are comparable with the lower redshift quasar absorption line technique (e.g., [Gauthier & Chen 2012](#); [Bordoloi et al. 2014a](#); [Kacprzak et al. 2014](#); [Schroetter et al. 2016, 2019](#); [Martin et al. 2019](#)), down-the-barrel observations (e.g., [Weiner et al. 2009](#); [Coil et al. 2011](#); [Martin et al. 2012](#); [Rubin et al. 2010, 2014](#)), and azimuthal angle distributions (e.g., [Bouché et al. 2012](#); [Kacprzak et al. 2012, 2015a](#); [Lan et al. 2014](#)).

These outflow characteristics are also consistent with the recent IllustrisTNG TNG50 simulations, where [Nelson et al. \(2019\)](#) examined supernovae- and black hole-driven outflows at  $z > 1$ . They found that  $T \sim 10^{4.5} \text{ K}$  gas (i.e., MgII) is confined to maximum outflow velocities of  $V_{\text{out}} < 500 \text{ km s}^{-1}$ , consistent with values we measure here. Collimation of the outflows was observed

by  $z = 1$ , where the gas was located along the galaxy minor axis with half opening angles of  $\theta_o = 40^\circ - 50^\circ$ , although the authors suggested collimation may not be strongly present at  $z = 2$  (also see [Steidel et al. 2010](#); [Law et al. 2012](#)). The maximum outflow velocity we constrained the model to,  $1000 \text{ km s}^{-1}$ , corresponds to very small half opening angles. This might indicate that the highest velocity gas possible for this system should be collimated in contrast to previous findings that found high velocities with low collimation (e.g., [Steidel et al. 2010](#)). It is difficult to further explore this scenario with the single absorber–galaxy pair studied here, especially since the modeled galaxy morphology parameters provide little constraint on the opening angles, i.e., the galaxy is assumed to be nearly perfectly edge-on ( $i = 85^\circ$ ) and probed along the minor axis ( $\Phi = 89^\circ$ ). A wider variety of galaxy morphologies will better constrain the typical  $z = 2$  outflow properties. Furthermore, a low collimation of outflows at these redshifts would mean that galaxy morphology is a less important gas flow diagnostic than at low redshift. In the case studied here, the uncertainty in the host galaxy’s morphology may not be important. This can be better tested with our forthcoming sample.

The timescales and ejection redshifts for the outflowing gas to reach the observed impact parameter of  $D = 66 \text{ kpc}$ ,  $t_{\text{out}} = 109 - 588 \text{ Myr}$  and  $z_{\text{eject}} = 2.15 - 2.55$ , are consistent with the timescales required for outflowing gas to recycle back onto galaxies (e.g., [Oppenheimer et al. 2010](#); [Anglés-Alcázar et al. 2017](#); although see [Keller et al. 2020](#)). They are also about 1 – 2 orders of magnitude larger than the lifetime of a starburst (e.g., [Thornley et al. 2000](#)). Given that the gas we observed is cool, photoionized material (at least for ions such as MgII, with  $T \sim 10^{4.5} \text{ K}$ ), it may be surprising that the gas has not yet been destroyed. Furthermore, [Crighton et al. \(2015\)](#) found that these clouds tend to be small, on the order of a few hundred parsecs (and even as small as  $\sim 10 \text{ pc}$ ; [Rigby et al. 2002](#)), sometimes characterized as circumgalactic “mist” or “fog” in simulations (e.g., [Liang & Remming 2020](#); [McCourt et al. 2018](#)), and so may be susceptible to being destroyed in an outflowing environment. Either the gas is being reformed as cool material condensing out of a hot halo (e.g., [Simcoe et al. 2006](#); [Fraternali et al. 2013](#)), or the clouds are embedded in progressively hotter phases (e.g., [Stern et al. 2016](#)). We support this latter scenario since we find multiphase gas with similar, but increasingly broader kinematics as the ionization state increases. This is particularly noticeable with the Si transitions: SiII, SiIII, and SiIV.

The final parameters obtained from the outflow modeling, mass outflow rates and mass loading factors, also

present an interesting picture of the outflowing gas from this galaxy. These values are  $\dot{M}_{\text{out}} < 52 \pm 37 \text{ M}_\odot \text{ yr}^{-1}$  and  $\eta < 1.4 \pm 1.0$ , implying an energetic and efficient outflow. In the SIMBA simulations ([Davé et al. 2019](#)), a typical star-forming galaxy similar to the galaxy we present here has a mass outflow rate of  $\dot{M}_{\text{out}} \sim 70 \text{ M}_\odot \text{ yr}^{-1}$  and  $\eta \sim 0.8$ , given a  $\text{SFR} \sim 85 \text{ M}_\odot \text{ yr}^{-1}$ . Our mass outflow rate and mass loading factor are comparable to the simulated galaxies as well as mass loading factors measured via a variety of estimators at low redshift (e.g., [Weiner et al. 2009](#); [Leethochawalit et al. 2019](#)).

Compared to most measurements from the  $z \sim 1$  quasar absorption line sample MEGAFLOW ([Schroetter et al. 2016, 2019](#)), who study stronger MgII absorbers with  $W_r(2796) \geq 0.5 \text{ Å}$ , our mass outflow rates are roughly an order of magnitude larger. This is likely due to the combination of less energetic/efficient outflows on average towards lower redshifts and the large uncertainties involved in measuring the total hydrogen column density. The few systems in their sample with comparable outflow rates to ours are also mostly located at  $D > 50 \text{ kpc}$ . The values we measure are also larger than the [Crighton et al. \(2015\)](#)  $z \sim 2.5$  outflow ( $\dot{M}_{\text{out}} = 5 \text{ M}_\odot \text{ yr}^{-1}$ ) at  $D = 50 \text{ kpc}$ , although the authors do not have galaxy morphologies in order to more accurately model the gas flows. A more comparable absorber–galaxy pair is the metal-rich outflow at  $z \sim 0.4$ ,  $D = 163 \text{ kpc}$  from [Muzahid et al. \(2015\)](#), which has an ultra-strong OVI absorption profile with  $\dot{M}_{\text{out}} \sim 54 \text{ M}_\odot \text{ yr}^{-1}$ . Most of these results are for absorbers located at fairly large impact parameter, which likely introduces additional uncertainty into the measurement since the gas could be destroyed as it moves out from the galaxy and the outflow velocities are likely not constant. Furthermore, the outflow likely sweeps up additional material as it plows through the CGM, so our values are better characterized as upper limits. Regardless, obtaining more  $z = 2 - 3$  measurements will better constrain the outflow properties to compare to the large number of  $z \lesssim 1$  systems.

There is still a non-zero probability that the galaxy is actually a major merging system. In this case, we might still observe outflowing material along the quasar sightline even if the J1430+014,  $z_{\text{gal}} = 2.0711$  object is a major merger. [Rupke et al. \(2019\)](#) studied a galactic wind in emission from a  $z \sim 0.459$  galaxy merger that is highly star-forming ( $\text{SFR} \sim 100 - 200 \text{ M}_\odot \text{ yr}^{-1}$ ; much further from the star formation main sequence than our galaxy). They identify bipolar outflow bubbles that are oriented perpendicular to the projected major axis of the object’s stellar component and most prominent tidal tail. Even though the projected major axis



of a merging system would be expected to change over time, the authors still found evidence for two outflow episodes as long as 0.4 Gyr and 7 Gyr ago with velocities  $> 100 \text{ km s}^{-1}$  within this emission structure. These timescales and velocities are consistent with the values measured for the J1430+014 object assuming a single edge-on galaxy.

#### 4.3. CGM Metallicity

The inferred total CGM metallicity along the line-of-sight for the J1430+014 absorber,  $[\text{Si}/\text{H}] = -1.5$ , is in the more metal-rich half of the pLLS/LLS distribution at  $z = 2-3$  (Lehner et al. 2016), which may favor an outflow scenario. With particle tracking, Hafen et al. (2019) examined the metallicities of accreting and outflowing gas at  $z = 2$  in the FIRE simulations and found that the median metallicity of outflowing gas is typically  $\sim 1$  dex larger than IGM accretion, with  $\log(Z/Z_{\odot}) \gtrsim -1.0$  for  $\log(M_{\text{h}}/M_{\odot}) > 11$ . The mass-metallicity relation for  $z \sim 2$  galaxies indicates that  $> L_{*}$  galaxies have gas-phase metallicities greater than  $-0.7$  dex below solar (Steidel et al. 2014; Kacprzak et al. 2015b; Sanders et al. 2015), and so any material ejected recently from the galaxy might be expected to have a similar metallicity. These values are more metal-rich than the metallicity we inferred for our absorber but we do not know the galaxy metallicity to determine how different the two values are.

The distribution of pLLS/LLS at  $z \sim 2$  suggests that CGM metallicities above  $[\text{X}/\text{H}] > -1.0$  are rare for systems like ours ( $\sim 13\%$ ; Lehner et al. 2016). However, outflows are ubiquitous around star-forming galaxies at  $z = 2-3$  (e.g., Steidel et al. 2010) and these outflows must be probed by quasar sightlines, so the lower CGM metallicity compared to the typical ISM metallicity is puzzling. Using the EAGLE and IllustrisTNG TNG50 simulations, Péroux et al. (2020) studied CGM metallicities as a function of azimuthal angle and found a constant metallicity of  $\sim -1.8$  for  $z = 2.4$  galaxies, which is slightly lower than our inferred value. Even though outflows are present in their simulations, there is no increase in the metal content for gas along the minor axis. The authors suggested that this was because galaxies at this epoch have not yet had enough time to enrich their CGM. Furthermore, low redshift observational studies have not yet demonstrated that minor axis gas, which should be dominated by outflows, has a CGM metallicity similar to the host galaxy ISM metallicity. At  $z \sim 0.3$  Kacprzak et al. (2019a) found that total CGM metallicities for minor axis sightlines are lower than ISM metallicities, with values on average  $-1.23$  dex below the ISM. Péroux et al. (2016) found a similar result and sug-

gested that the gas was ejected from the galaxy before it had been sufficiently processed by stars to increase the metal content, which could also be expected for highly star-forming galaxies at  $z \sim 2$ .

Given the gas we observe is  $D = 66$  kpc from the galaxy and has had to travel through the CGM along the way, it is also likely that the outflow has entrained more metal-poor material from accretion, past outflows, and/or other CGM material and resulted in a lower metallicity. Thus while the current metallicity might indicate the gas is not completely new metal-rich material from the current star formation activity, we can conclude that the gas had been in the galaxy at some point in the past and was likely ejected via an outflow. It is relevant to note that we assume a single low ionization phase when inferring a metallicity, so we may be missing outflow mass if metal-rich outflows are primarily hot, high ionization material (e.g., Muzahid et al. 2015). The lower metallicity, low ionization gas we observe would then be an indirect tracer of these outflows as entrained material and provide more accurate information about the kinematics and spatial distribution of the outflow than the metallicity.

A troublesome aspect of inferring a total CGM metallicity is that observations have not yet convincingly demonstrated that metallicity is a good discriminator between accreting and outflowing gas for a large sample of galaxies. The typical method for inferring a total metallicity neglects the effects of dust depletion, as we have done here. Wendt et al. (2020) found that minor axis sightlines have increased amounts of dust, which would result in lower inferred metallicities if dust is not accounted for, so our inferred value could be artificially low. Additionally, the CGM is expected to be messy, with the various baryon cycle processes mixing at all radii (at least for  $z < 1$ ; Péroux et al. 2016; Pointon et al. 2019; Kacprzak et al. 2019a). In fact, simulations often show that quasar sightlines pass through multiple structures along the line-of-sight (Churchill et al. 2015; Kacprzak et al. 2019b; Peebles et al. 2019), making total CGM metallicities an insensitive probe of gas flows. Hafen et al. (2019) suggested that the CGM becomes more well-mixed towards lower redshift, further complicating the metallicities measured observationally (also see Hafen et al. 2017). For the J1430+014 absorber studied here, we do see varying ionization conditions (and likely metallicities) across the profile, particularly when comparing SiII, SiIII, and SiIV in the bluest components. This further supports the discussion in the previous paragraph that the observed gas may not be purely outflow material but either represents an outflow that has swept up additional material on its way

through the CGM, or the nature of quasar sightlines means we are probing a very large range in radius from the galaxy so that the sightline passes through multiple separate structures with different ionization conditions and metallicities. In contrast, [Veilleux et al. \(2005\)](#) suggest that large variations in metallicity and ionization conditions between clouds across an absorption profile might be a signature of outflows in addition to broad complex kinematics spanning a few hundred  $\text{km s}^{-1}$ , kinematics that are not consistent with rotation,  $\alpha$ -rich abundances, and dual-trough absorption with weak absorption between. There are few studies thus far with detailed metallicity and kinematic analyses in order to investigate this further.

To improve the metallicity measurement and better determine the structures along the line-of-sight, a multiphase and multicomponent modeling approach would be best. Several works have done such a study and found differing metallicities in each component and/or phase (e.g., [Tripp et al. 2011](#); [Crighton et al. 2015, 2016](#); [Muzahid et al. 2015, 2016](#); [Rosenwasser et al. 2018](#); [Zahedy et al. 2019a](#)) and these insights could be used to determine if outflows, inflows, tidal material, etc., are present along the same sightline. In particular, a multiphase analysis would provide insights into whether outflows are primarily traced by hot high ionization gas with metallicities similar to the galaxy ISM metallicity and whether the lower ions along the same sightline trace cooler, more metal-poor gas entrained by the hot outflow, which is a possible solution to the total metallicity problem suggested by [Kacprzak et al. \(2019a\)](#) that might fit the scenario we observe here. The difficulty with this method is that it requires partitioning each ion between VP components and phases, and modeling a consistent set of VP components across transitions with similar ionization phase. This is particularly challenging when absorption is saturated and the selection of lines is limited, i.e., the only H I line observed is saturated as in the system presented here. While much of our sample has coverage of multiple H I Lyman series lines and in some cases the full series to properly do a multiphase and multicomponent analysis, the J1430+014,  $z = 2.071$  absorber is not a good candidate for this method. Without obtaining new spectra to better cover the H I Lyman series, we would need to make assumptions on how to partition the saturated H I between components and phases, which would result in over-interpreting the absorption. Furthermore, the vast majority of metallicities in the literature are total metallicities. To study the evolution of the CGM from Cosmic Noon to today, we have focused on total metallicities here.

Even though metallicity is a useful diagnostic for ruling out some scenarios of gas flow origins, especially at higher redshift where CGM mixing appears to be less efficient, a variety of properties such as kinematics and galaxy morphologies must also be considered for a more accurate picture, which we have done here. This approach has thus far only been done a few times at Cosmic Noon.

#### 4.4. Other Gas Flow Interpretations

Other mechanisms and structures that could give rise to the observed absorption include tidal streams (e.g., [Yun et al. 1994](#); [Chynoweth et al. 2008](#); [Kacprzak et al. 2010b](#); [Duc & Renaud 2013](#); [de Blok et al. 2018](#)), IGM accretion (e.g., [Birnboim & Dekel 2003](#); [Kereš et al. 2005](#)), an intragroup medium (e.g., [Whiting et al. 2006](#); [Kacprzak et al. 2010b](#); [Bielby et al. 2017](#); [Péroux et al. 2017](#); [Pointon et al. 2017](#); [Nielsen et al. 2018](#); [Chen et al. 2019](#); [Hamanowicz et al. 2020](#)), and intergalactic transfer (e.g., [Anglés-Alcázar et al. 2017](#)).

##### 4.4.1. Tidal Stripping in a Major Merger

While we have made the assumption throughout the paper that the galaxy is a single, clumpy, edge-on disk, it has a non-zero probability of being a major merger system in the late stages of merging (see Section 4.1). In this case, the absorbing gas observed in the quasar spectrum could be tidal debris from the merging process. Observations suggest that thin tidal streams extend out to  $\sim 40$  kpc in the M81/M82 system (e.g., [Yun et al. 1994](#); [de Blok et al. 2018](#)),  $\sim 80$  kpc in the Antennae galaxies (NGC4038/9, e.g., [Schweizer 1978](#); [Hibbard et al. 2001](#)), potentially beyond  $\sim 100$  kpc in other systems/simulations (see [Duc & Renaud 2013](#), for a review), and are even visible out to at least  $\sim 25$  kpc in *HST* imaging and MUSE observations of galaxies hosting CGM absorbers (Q1127–145, e.g., [Kacprzak et al. 2010b](#); [Péroux et al. 2017](#); [Chen et al. 2019](#)). [Hani et al. \(2018\)](#) studied the impact a simulated major merger has on the CGM at  $z < 1$  by investigating the velocities, column density profiles, covering fractions, and enrichment of the CGM before, during, and after a merging event between two  $\log(M_*/M_\odot) \sim 10$  galaxies in the Illustris simulations. They found that stellar tidal streams are not observed beyond 50 kpc throughout the merging process, but that the velocity field of the gas at large impact parameter supports an outflow origin. The authors suggested that tidal stripping is not a primary mechanism for distributing material into the CGM during a major merger, at least beyond 50 kpc. This is further corroborated in the FIRE simulations, where  $z = 2$  galaxies have gas flows that are dominated by fresh ac-

cretion and wind recycling ( $> 70\%$ ), with a minor contribution from mergers (Anglés-Alcázar et al. 2017).

To better understand the contributions of tidal stripping and outflows in a major merger, we estimated covering fractions of gas in the two scenarios. In the first scenario, we assume that a major merger would have tidal streams similar to those found in the Antennae galaxies, with a radial extent of  $\sim 80$  kpc and a thickness of  $\sim 15$  kpc (Schweizer 1978; Hibbard et al. 2001). Assuming that there are two tidal streams crossing a projected distance from a merging system of  $D \sim 70$  kpc (the rough impact parameter of our absorber–galaxy pair at  $z = 2.071$ ) and the streams themselves have a unity covering fraction, we estimate a total tidal stream covering fraction at 70 kpc of only 7%. This value could be larger if the tidal streams are wider or cross the boundary multiple times (i.e., doubling the width increases the covering fraction to 14% and additionally having both thicker streams cross the 70 kpc twice increases the value to 28%), but could also be smaller if the streams are thinner, one or both of the streams do not reach the impact parameter in question, and/or the streams themselves have less than unity covering fraction. In the second scenario, if we assume that bipolar outflowing gas has a unity covering fraction within the outflow cones, then we find a total outflow covering fraction at 70 kpc ranging between 16% for a half opening angle of  $14^\circ$  and 83% for a half opening angle of  $75^\circ$ , where the half opening angles are the allowed bounds for J1430+014,  $z_{\text{gal}} = 2.0711$  from Table 5. While the total outflow covering fraction could be smaller with a lower covering fraction within the outflow itself and if some of the material does not reach  $D \sim 70$  kpc, there is evidence that outflowing gas is not well-collimated at  $z \sim 2$  (e.g., Steidel et al. 2010; Law et al. 2012; Nelson et al. 2019). This suggests that the total outflow covering fraction is more likely to be on the higher side of the estimated range. Despite the presence of both tidal streams and outflowing gas in the CGM surrounding a major merger, the probability of intersecting outflowing gas is much higher than the thin filamentary tidal material.

The simulations, the large impact parameter of the absorber–galaxy pair studied here, the low covering fraction of tidal material, the high covering fraction of outflowing material, and the similarity to the outflows discovered in Makani (Rupke et al. 2019) further suggest that the absorption we measure in the CGM of the J1430+014,  $z_{\text{gal}} = 2.0711$  galaxy is more likely outflowing material even if the morphology is a major merger rather than an edge-on disk.

#### 4.4.2. IGM Accretion

We rule out IGM accretion as the dominant source of the gas for several different reasons. First, IGM accretion is expected to have a low metallicity (van de Voort & Schaye 2012; Hafen et al. 2019) but the gas we observe is relatively metal-enriched compared to the distribution of  $z = 2 - 3$  LLSs. Second, accreting IGM filaments are expected to add angular momentum to the host galaxy (Danovich et al. 2012, 2015), which implies that the gas must align with the star forming disk and be offset in velocity towards one side (Stewart et al. 2011, 2013, 2017). Recall that the gas studied here is located along the minor axis of its host galaxy, where an accreting filament of gas is unlikely to be directly perpendicular to the disk even at the somewhat large impact parameter ( $D = 66$  kpc). Also, the gas spans both sides of the systemic galaxy velocity, in contradiction to predictions and major axis observations (Kacprzak et al. 2011; Ho et al. 2017). Third, accreting filaments are expected to have small cross-sections, at least at low redshift, and have yet to be directly observed. While it is possible that accretion has larger cross-sections at Cosmic Noon when the process is most active, the combination with the other two points makes it unlikely that we have observed accreting material in the first galaxy studied for our survey without specifically searching for its signatures.

#### 4.4.3. Group Environments and Intergalactic Transfer

It is possible that this absorber is located in a group environment given the proximity of three additional galaxies in projection on the sky in the *HST* image. However, we detect no obvious  $\text{Ly}\alpha$  emission, or any other lines consistent with a  $z = 2$  LBG, from these three galaxies. The  $\text{Ly}\alpha$  emission in the continuum galaxy spectrum (bottom panels of Figure 4) appears to be contamination from the host galaxy. This could be due to the seeing ( $\text{FWHM} \sim 1''$ ) and/or  $\text{Ly}\alpha$  emission in the CGM of the  $z = 2.0711$  host galaxy detailed here. At  $z > 3$  Leclercq et al. (2017) studied the  $\text{Ly}\alpha$  emission profiles around star-forming galaxies with VLT/MUSE. The authors found that  $\text{Ly}\alpha$  emission halos are ubiquitous around star-forming galaxies, with 80% of their sample of  $\sim 150$  galaxies having firmly measured  $\text{Ly}\alpha$  emission extending out to scale lengths of roughly  $4 - 5$  kpc and even beyond 10 kpc (also see Xue et al. 2017). The distance between our CGM host galaxy and the non-related continuum galaxy with contaminating  $\text{Ly}\alpha$  emission is roughly  $1''8$ , corresponding to  $D = 15$  kpc, and is consistent with the scale lengths measured.

At low redshift, group environments have a differential influence on the various metal lines we observe in this system. Group environments appear to enhance low ionization lines such as MgII to a degree, where the equivalent widths and radial extent are larger, and kinematic spreads are comparable to outflows for small galaxy–galaxy groups (e.g., Bordoloi et al. 2011; Nielsen et al. 2018). The strongest MgII absorbers may also be located in group environments (Nestor et al. 2007, 2011; Gauthier 2013). For more dense group environments and cluster environments, a dearth of low equivalent width MgII absorbers and a smaller radial extent of the gas indicates that the cluster environments are hot enough to ionize the gas to higher phases (e.g., Lopez et al. 2008; Padilla et al. 2009; Andrews et al. 2013). The MgII observed here is fairly weak, but its kinematics still appear to be consistent with outflows. In contrast, the intermediate and higher ions such as CIV and OVI are more easily ionized to higher states in group environments (e.g., Burchett et al. 2016, 2018; Pointon et al. 2017; Ng et al. 2019), where the detection rate drops with an increasing density of the environment. Given that the CIV observed in this system is strong and the MgII is not enhanced, a group environment seems less likely.

The CGM host galaxy is clearly a Ly $\alpha$  emitter, which is more likely located in the distant outskirts of group environments (where group interactions are minimal) or is isolated (Cooke et al. 2013). While this may rule out nearby large galaxies, it does not rule out the possibility that this gas is falling onto the host galaxy from a satellite experiencing active star formation. Given the redshift and the large KCWI spaxels ( $\sim 2 - 6$  kpc), we cannot detect satellite galaxies surrounding the bright host. It is possible that satellites may be detected by examining the Ly $\alpha$  emission halo in detail, which may be clumpy and asymmetric when strong Ly $\alpha$ -emitting satellites are present (Leclercq et al. 2017). Unfortunately our KCWI data are not of sufficiently high spatial resolution to investigate this further. Despite all this, it is less likely that this scenario dominates the absorption signal due to the small cross-sections expected (Gauthier et al. 2010; Martin et al. 2012; Tumlinson et al. 2013). The transfer of material between galaxies in this scenario is expected to dominate over other gas flows only at lower redshift, with only  $< 10\%$  of gas flows at  $z = 2$  coming from intergalactic transfer in the FIRE simulations (Anglés-Alcázar et al. 2017). The galaxies in these simulations are instead dominated by wind recycling and fresh accretion at  $z = 2$ , which comprise  $> 70\%$  of gas flows.

Under the assumption that the object we observe with Ly $\alpha$  is a single, clumpy, edge-on galaxy on the SFR main sequence, the scientific evidence best supports an interpretation that the observed absorption is an outflow from an isolated galaxy at Cosmic Noon that has likely swept up more metal-poor CGM material as it moves away from the galaxy. With only a few  $z = 2 - 3$  absorber–galaxy pairs with galaxy morphologies and CGM metallicities, it is difficult to make any conclusions about the general properties of the CGM or outflows during this epoch. However, we aim to build a sample of  $\sim 50$  MgII absorber–galaxy pairs with similar quality data and with coverage of other ions for comparison to the low redshift, multiphase CGM.

## 5. SUMMARY AND CONCLUSIONS

We presented the first results from our CGM at Cosmic Noon with KCWI program: minor axis gas that is likely outflowing and sweeping up additional more metal-poor CGM material from a  $z_{\text{gal}} = 2.0711$  star-forming galaxy in quasar field J143040+014939. The program was designed by identifying quasar fields with MgII absorbers at  $1.9 < z_{\text{abs}} < 2.6$  in Keck/HIRES or VLT/UVES spectra and required that each field have existing *HST* (ACS, WFPC2, and/or WFC3) or Keck/NIRC2-LGSAO imaging for galaxy morphology modeling. We then observed each field with KCWI to search for the host galaxies in Ly $\alpha$  emission. From an analysis on a single absorber–galaxy pair in the J1430+014 field, our results include the following:

1. We identified the absorbing host galaxy with Ly $\alpha$  emission at  $z_{\text{gal}} = 2.0711 \pm 0.0003$  in the KCWI datacube  $D = 66$  kpc away from the quasar sightline. The galaxy is isolated and star-forming with  $\text{SFR}_{\text{FUV}} = 37.8 \text{ M}_{\odot} \text{ yr}^{-1}$ . It has a clumpy morphology, which is typical of  $z = 2 - 3$  star-forming galaxies, and we assume an edge-on ( $i = 85^{\circ}_{-2}^{+5}$ ) inclination based on the object’s small size, small clump separation, and main sequence SFR. A major merger morphology is also possible, but less likely given these characteristics. The quasar sightline probes the galaxy along the projected minor axis ( $\Phi = 89^{\circ}_{-5}^{+1}$ ). The Ly $\alpha$  emission halo surrounding the galaxy appears to extend out to at least  $1''.8$ , corresponding to  $D \sim 15$  kpc.
2. The absorption system is roughly centered at the host galaxy systemic velocity, with an average offset of  $\Delta v_{\text{gal-abs}} = -27 \text{ km s}^{-1}$ . The full MgII velocity spread of  $\Delta v \sim 210 \text{ km s}^{-1}$  means that the absorption spans both sides of the galaxy systemic velocity. The absorption is multiphase, with



detected Ly $\alpha$ , MgII, SiII, SiIII, SiIV, CII, and CIV, where Ly $\alpha$  and the higher ions have larger velocity spreads. We constrain the H I column density from only the saturated Ly $\alpha$  absorption line to the range  $15.00 \leq \log N_{\text{H I}} \leq 18.18 \text{ cm}^{-2}$ , indicating that this is a pLLS/LLS. The MgII equivalent width,  $W_r(2796) = 0.24 \pm 0.01 \text{ \AA}$ , places this absorber–galaxy pair in line with the  $W_r(2796) - D$  anti-correlation and within uncertainties of the log-linear fit to the anti-correlation from Nielsen et al. (2013a,b) at  $z < 1$ . For this single absorber, this indicates that there is no clear evolution of the CGM extent from low redshift.

3. From photoionization modeling, the total CGM metallicity is inferred to be  $[\text{Si}/\text{H}] = -1.5^{+0.4}_{-0.3}$ , which is slightly more metal-rich than the peak in the distribution of pLLSs/LLSs metallicities at  $z = 2 - 3$ , but is lower than the metallicities expected for purely outflowing gas at this epoch. Assuming the gas is an outflow, this lower metallicity is not unexpected since outflows likely entrain more metal-poor CGM gas from past outflows on their way out from the galaxy, especially to  $D = 66 \text{ kpc}$ . The ionization conditions, and therefore the metallicities, appear to vary across the absorption profile, which may be a signature of outflows, but the lack of additional H I Lyman series lines for this system prevents further robust analyses to investigate this. Removing higher ionization ions such as CIV and NV from the photoionization modeling to account for possible multiphase structure does not significantly change the inferred value, but does suggest the true value could be 0.3 dex more metal-poor.
4. The metal line absorption kinematics are comparable to those found in the Milky Way Fermi bubbles, where the bulk of the absorption is centered on  $z_{\text{gal}}$  with roughly symmetric higher velocity components (Fox et al. 2015). Under the assumption that the host galaxy has an edge-on inclination, modeling the MgII kinematics as a biconical outflow suggests that the gas is a decelerating outflow, where we constrain the average radial outflow velocities over the range of  $V_{\text{out}} \sim 109 - 588 \text{ km s}^{-1}$  for half opening angles of  $\theta_0 \sim 14^\circ - 75^\circ$ . Assuming a constant outflow velocity, it would take on average  $\sim 111 - 597 \text{ Myr}$  for the gas to reach 66 kpc, corresponding to gas ejection redshifts between  $z_{\text{eject}} \sim 2.15 - 2.55$ . This is enough time for the galaxy to evolve from higher SFRs when the observed gas was ejected in an out-

flow to the SFR we measure at  $D = 66 \text{ kpc}$  and  $z_{\text{gal}} = 2.0711$ .

5. Assuming the gas is outflowing, we measure mass outflow rates of  $\dot{M}_{\text{out}} \lesssim 52 \pm 37 \text{ M}_\odot \text{ yr}^{-1}$ . Given this range, the mass loading factors are  $\eta \lesssim 1.4 \pm 1.0$ . These values are comparable to simulated galaxies of similar magnitude. They are also roughly an order of magnitude larger than those measured at  $z \sim 1$  with the MEGAFLOW survey (Schroetter et al. 2016, 2019) but are comparable to those measured in an extreme metal-rich outflow at  $z = 0.4$  (Muzahid et al. 2015). The outflow from this galaxy at Cosmic Noon may be more energetic and more efficient than those at lower redshifts but this is not yet well-constrained.
6. Other gas flow origins such as tidal streams, IGM accretion, and an intragroup medium with intergalactic transfer do not appear to explain the observed properties of the absorption and its relation to the host galaxy as well as an outflow origin, nor are they as probable. While an outflow best fits the gas kinematics and quasar–galaxy orientation, the outflow has likely swept up additional more metal-poor material from accretion and/or past outflows on its way through the CGM.
7. We caution against making strong interpretations as to the origin of CGM material based solely on total metallicity with the data and analyses available since lower redshift work has not yet convincingly demonstrated that total metallicities separate out accretion and outflows. Our outflow interpretation here was determined based on evidence that the galaxy is on the star formation rate main sequence, has an edge-on inclination, the quasar probes the galaxy projected minor axis, the broad absorber kinematics that are roughly symmetrically centered on  $z_{\text{gal}}$ , and more cautiously, a total metallicity in the upper half of the pLLS/LLS distribution. A multiphase and multicomponent metallicity analysis may be more robust for determining whether the ionization structure across the absorption profile is indicative of outflows or multiple structures along the quasar sightline, but this is not possible here due to the lack of additional non-saturated H I transitions.

These first results show how powerful the combination of high-resolution quasar spectra, *HST* images, and KCWI integral field spectroscopy is for studying the CGM at Cosmic Noon. We have examined the gas flow properties in as much detail as has been done at

$z < 1$  for a single absorber–galaxy pair and this is one of only a few systems at this epoch with this wealth of data, specifically including galaxy morphologies and CGM metallicities. In the future, we plan to compile a sample of roughly 50  $z = 2-3$  absorber–galaxy pairs for not only detailed single system studies, but also ensemble studies, which can then be compared to those at low redshift to study how gas flows evolve over ten billion years.

### ACKNOWLEDGMENTS

We thank the anonymous referees for comments that improved this manuscript. N.M.N. thanks L. Rizzi, G. Doppmann, J. O’Meara, A. Ferré-Mateu, S. Cantalupo, and D. Rupke for useful KCWI discussions, and J. Cooke, T. Yuan, and D. B. Fisher for high redshift galaxy discussions.

N.M.N., G.G.K., and M.T.M. acknowledge the support of the Australian Research Council through *Discovery Project* grant DP170103470. Parts of this research were supported by the Australian Research Council Centre of Excellence for All Sky Astrophysics in 3 Dimensions (ASTRO 3D), through project number CE170100013. C.W.C. was supported by the National Science Foundation through grant NSF AST-1517816 and by NASA through HST grant GO-13398 from the

Space Telescope Science Institute, which is operated by the Association of Universities for Research in Astronomy, Inc., under NASA contract NAS5-26555.

Some of the data presented herein were obtained at the W. M. Keck Observatory, which is operated as a scientific partnership among the California Institute of Technology, the University of California and the National Aeronautics and Space Administration. The Observatory was made possible by the generous financial support of the W. M. Keck Foundation. Observations were supported by Swinburne Keck programs with KCWI: 2017B\_W270, 2018A\_W185, 2018B\_W232; with NIRC2-LGSAO: 2019B\_W237; and NASA Keck program with KCWI: 2020B\_N021. The authors wish to recognize and acknowledge the very significant cultural role and reverence that the summit of Maunakea has always had within the indigenous Hawaiian community. We are most fortunate to have the opportunity to conduct observations from this mountain.

*Facilities:* Keck:II (KCWI), VLT:Kueyen (UVES), *HST* (ACS)

*Software:* Astropy (Astropy Collaboration et al. 2013), Cloudy (Ferland et al. 2013), Matplotlib (Hunter 2007), numpy (Harris et al. 2020), PyAstronomy, scipy (Jones et al. 2001), qfitsview, VPFIT (Carswell & Webb 2014)

### REFERENCES

- Allen, R. J., Kacprzak, G. G., Glazebrook, K., et al. 2017, *ApJ*, 834, L11
- Andrews, H., Barrientos, L. F., López, S., et al. 2013, *ApJ*, 774, 40
- Anglés-Alcázar, D., Faucher-Giguère, C.-A., Kereš, D., et al. 2017, *MNRAS*, 470, 4698
- Astropy Collaboration, Robitaille, T. P., Tollerud, E. J., et al. 2013, *A&A*, 558, A33
- Bertin, E., & Arnouts, S. 1996, *Astronomy and Astrophysics Supplement Series*, 117, 393
- Bielby, R., Crighton, N. H. M., Fumagalli, M., et al. 2017, *MNRAS*, 468, 1373
- Birnboim, Y., & Dekel, A. 2003, *MNRAS*, 345, 349
- Bordoloi, R., Lilly, S. J., Kacprzak, G. G., & Churchill, C. W. 2014a, *ApJ*, 784, 108
- Bordoloi, R., Lilly, S. J., Knobel, C., et al. 2011, *ApJ*, 743, 10
- Bordoloi, R., Lilly, S. J., Hardmeier, E., et al. 2014b, *ApJ*, 794, 130
- Bordoloi, R., Fox, A. J., Lockman, F. J., et al. 2017, *ApJ*, 834, 191
- Bouché, N., Hohensee, W., Vargas, R., et al. 2012, *MNRAS*, 426, 801
- Bouché, N., Murphy, M. T., Kacprzak, G. G., et al. 2013, *Science*, 341, 50
- Burchett, J. N., Rubin, K. H. R., Prochaska, J. X., et al. 2020, arXiv e-prints, [arXiv:2005.03017](https://arxiv.org/abs/2005.03017)
- Burchett, J. N., Tripp, T. M., Wang, Q. D., et al. 2018, *MNRAS*, 475, 2067
- Burchett, J. N., Tripp, T. M., Bordoloi, R., et al. 2016, *ApJ*, 832, 124
- Carswell, R. F., & Webb, J. K. 2014, VPFIT: Voigt profile fitting program, Astrophysics Source Code Library
- Chen, H.-W. 2012, *MNRAS*, 427, 1238
- Chen, H.-W., Boettcher, E., Johnson, S. D., et al. 2019, *ApJL*, 878, L33
- Chen, H.-W., Johnson, S. D., Zahedy, F. S., Rauch, M., & Mulchaey, J. S. 2017, *ApJ*, 842, L19
- Chen, Y., Steidel, C. C., Hummels, C. B., et al. 2020, *MNRAS*
- Churchill, C. W., Evans, J. L., Stemmock, B., et al. 2020, arXiv e-prints, [arXiv:2008.08487](https://arxiv.org/abs/2008.08487)

- Churchill, C. W., Vander Vliet, J. R., Trujillo-Gomez, S., Kacprzak, G. G., & Klypin, A. 2015, *ApJ*, **802**, 10
- Churchill, C. W., Vogt, S. S., & Charlton, J. C. 2003, *AJ*, **125**, 98
- Chynoweth, K. M., Langston, G. I., Yun, M. S., et al. 2008, *AJ*, **135**, 1983
- Coil, A. L., Weiner, B. J., Holz, D. E., et al. 2011, *ApJ*, **743**, 46
- Cooke, J., Omori, Y., & Ryan-Weber, E. V. 2013, *MNRAS*, **433**, 2122
- Cooke, J., Wolfe, A. M., Gawiser, E., & Prochaska, J. X. 2006, *ApJ*, **652**, 994
- Cooke, J., Wolfe, A. M., Prochaska, J. X., & Gawiser, E. 2005, *ApJ*, **621**, 596
- Cooper, T. J., Simcoe, R. A., Cooksey, K. L., O’Meara, J. M., & Torrey, P. 2015, *ApJ*, **812**, 58
- Crighton, N. H. M., Hennawi, J. F., & Prochaska, J. X. 2013, *ApJL*, **776**, L18
- Crighton, N. H. M., Hennawi, J. F., Simcoe, R. A., et al. 2015, *MNRAS*, **446**, 18
- Crighton, N. H. M., O’Meara, J. M., & Murphy, M. T. 2016, *MNRAS*, **457**, L44
- Daddi, E., Dickinson, M., Morrison, G., et al. 2007, *ApJ*, **670**, 156
- Danovich, M., Dekel, A., Hahn, O., Ceverino, D., & Primack, J. 2015, *MNRAS*, **449**, 2087
- Danovich, M., Dekel, A., Hahn, O., & Teyssier, R. 2012, *MNRAS*, **422**, 1732
- Davé, R., Anglés-Alcázar, D., Narayanan, D., et al. 2019, *MNRAS*, **486**, 2827
- de Blok, W. J. G., Walter, F., Ferguson, A. M. N., et al. 2018, *ApJ*, **865**, 26
- Dekker, H., D’Odorico, S., Kaufer, A., Delabre, B., & Kotzlowski, H. 2000, in SPIE Conference Series, Vol. 4008, Optical and IR Telescope Instrumentation and Detectors, ed. M. Iye & A. F. Moorwood, 534–545
- Duc, P.-A., & Renaud, F. 2013, Tides in Colliding Galaxies, ed. J. Souchay, S. Mathis, & T. Tokieda, Vol. 861, 327
- Dutta, R., Fumagalli, M., Fossati, M., et al. 2020, arXiv e-prints, [arXiv:2009.14219](https://arxiv.org/abs/2009.14219)
- Elmegreen, D. M., Elmegreen, B. G., Ravindranath, S., & Coe, D. A. 2007, *ApJ*, **658**, 763
- Evans, J. L. 2011, PhD thesis, New Mexico State University
- Ferland, G. J., Porter, R. L., van Hoof, P. A. M., et al. 2013, *RMxAA*, **49**, 137
- Fisher, D. B., Glazebrook, K., Damjanov, I., et al. 2017, *MNRAS*, **464**, 491
- Foreman-Mackey, D., Hogg, D. W., Lang, D., & Goodman, J. 2013, *PASP*, **125**, 306
- Fox, A. J., Bordoloi, R., Savage, B. D., et al. 2015, *ApJL*, **799**, L7
- Fraternali, F., Marasco, A., Marinacci, F., & Binney, J. 2013, *ApJL*, **764**, L21
- Fumagalli, M., O’Meara, J. M., & Prochaska, J. X. 2016, *MNRAS*, **455**, 4100
- Gabasch, A., Bender, R., Seitz, S., et al. 2004, *A&A*, **421**, 41
- Gauthier, J.-R. 2013, *MNRAS*, **432**, 1444
- Gauthier, J.-R., & Chen, H.-W. 2012, *MNRAS*, **424**, 1952
- Gauthier, J.-R., Chen, H.-W., & Tinker, J. L. 2010, *ApJ*, **716**, 1263
- Gonzaga, S., Hack, W., Fruchter, A., Mack, J., & et al. 2012, The DrizzlePac Handbook
- Guo, Y., Ferguson, H. C., Bell, E. F., et al. 2015, *ApJ*, **800**, 39
- Haardt, F., & Madau, P. 2001, in Clusters of Galaxies and the High Redshift Universe Observed in X-rays, ed. D. M. Neumann & J. T. V. Tran, 64
- Haardt, F., & Madau, P. 2012, *ApJ*, **746**, 125
- Hafen, Z., Faucher-Giguère, C.-A., Anglés-Alcázar, D., et al. 2017, *MNRAS*, **469**, 2292
- . 2019, *MNRAS*, **488**, 1248
- Hamanowicz, A., Péroux, C., Zwaan, M. A., et al. 2020, *MNRAS*, **492**, 2347
- Hani, M. H., Sparre, M., Ellison, S. L., Torrey, P., & Vogelsberger, M. 2018, *MNRAS*, **475**, 1160
- Hao, C.-N., Kennicutt, R. C., Johnson, B. D., et al. 2011, *ApJ*, **741**, 124
- Harris, C. R., Millman, K. J., van der Walt, S. J., et al. 2020, *Nature*, **585**, 357–362
- Hasan, F., Churchill, C. W., Stemock, B., et al. 2020, arXiv e-prints, [arXiv:2007.11751](https://arxiv.org/abs/2007.11751)
- Hibbard, J. E., van der Hulst, J. M., Barnes, J. E., & Rich, R. M. 2001, *AJ*, **122**, 2969
- Ho, S. H., & Martin, C. L. 2020, *ApJ*, **888**, 14
- Ho, S. H., Martin, C. L., Kacprzak, G. G., & Churchill, C. W. 2017, *ApJ*, **835**, 267
- Hung, C.-L., Rich, J. A., Yuan, T., et al. 2015, *ApJ*, **803**, 62
- Hunter, J. D. 2007, *Computing in Science Engineering*, **9**, 90-95
- Jones, E., Oliphant, T., Peterson, P., et al. 2001, SciPy: Open source scientific tools for Python. <http://www.scipy.org/>
- Kacprzak, G. G., Churchill, C. W., Barton, E. J., & Cooke, J. 2011, *ApJ*, **733**, 105
- Kacprzak, G. G., Churchill, C. W., Ceverino, D., et al. 2010a, *ApJ*, **711**, 533
- Kacprzak, G. G., Churchill, C. W., & Nielsen, N. M. 2012, *ApJL*, **760**, L7
- Kacprzak, G. G., Murphy, M. T., & Churchill, C. W. 2010b, *MNRAS*, **406**, 445
- Kacprzak, G. G., Muzahid, S., Churchill, C. W., Nielsen, N. M., & Charlton, J. C. 2015a, *ApJ*, **815**, 22
- Kacprzak, G. G., Pointon, S. K., Nielsen, N. M., et al. 2019a, *ApJ*, **886**, 91
- Kacprzak, G. G., Martin, C. L., Bouché, N., et al. 2014, *ApJL*, **792**, L12

- Kacprzak, G. G., Yuan, T., Nanayakkara, T., et al. 2015b, *ApJL*, **802**, L26
- Kacprzak, G. G., Vander Vliet, J. R., Nielsen, N. M., et al. 2019b, *ApJ*, **870**, 137
- Keller, B. W., Kruijssen, J. M. D., & Wadsley, J. W. 2020, *MNRAS*, **493**, 2149
- Kereš, D., Katz, N., Weinberg, D. H., & Davé, R. 2005, *MNRAS*, **363**, 2
- Krist, J. E., Hook, R. N., & Stoehr, F. 2011, in Society of Photo-Optical Instrumentation Engineers (SPIE) Conference Series, Vol. 8127, Optical Modeling and Performance Predictions V, 81270J
- Krogager, J.-K., Fynbo, J. P. U., Ledoux, C., et al. 2013, *MNRAS*, **433**, 3091
- Lan, T.-W., Ménard, B., & Zhu, G. 2014, *ApJ*, **795**, 31
- Lan, T.-W., & Mo, H. 2018, *ApJ*, **866**, 36
- Law, D. R., Steidel, C. C., Shapley, A. E., et al. 2012, *ApJ*, **759**, 29
- Leclercq, F., Bacon, R., Wisotzki, L., et al. 2017, *A&A*, **608**, A8
- Leethochawalit, N., Kirby, E. N., Ellis, R. S., Moran, S. M., & Treu, T. 2019, *ApJ*, **885**, 100
- Lehner, N., O’Meara, J. M., Fox, A. J., et al. 2014, *ApJ*, **788**, 119
- Lehner, N., O’Meara, J. M., Howk, J. C., Prochaska, J. X., & Fumagalli, M. 2016, *ApJ*, **833**, 283
- Lehner, N., Wotta, C. B., Howk, J. C., et al. 2019, *ApJ*, **887**, 5
- Lehner, N., Howk, J. C., Tripp, T. M., et al. 2013, *ApJ*, **770**, 138
- Liang, C. J., & Remming, I. 2020, *MNRAS*, **491**, 5056
- Lilly, S. J., Carollo, C. M., Pipino, A., Renzini, A., & Peng, Y. 2013, *ApJ*, **772**, 119
- Lopez, S., Barrientos, L. F., Lira, P., et al. 2008, *ApJ*, **679**, 1144
- Lopez, S., Tejos, N., Ledoux, C., et al. 2018, *Nature*, **554**, 493
- Lopez, S., Tejos, N., Barrientos, L. F., et al. 2020, *MNRAS*, **491**, 4442
- Madau, P., & Dickinson, M. 2014, *ARA&A*, **52**, 415
- Martin, C. L., Ho, S. H., Kacprzak, G. G., & Churchill, C. W. 2019, *ApJ*, **878**, 84
- Martin, C. L., Shapley, A. E., Coil, A. L., et al. 2012, *ApJ*, **760**, 127
- Mathes, N. L., Churchill, C. W., & Murphy, M. T. 2017, arXiv e-prints, [arXiv:1701.05624](https://arxiv.org/abs/1701.05624)
- Matthee, J., Sobral, D., Best, P., et al. 2017, *MNRAS*, **465**, 3637
- McCourt, M., Oh, S. P., O’Leary, R., & Madigan, A.-M. 2018, *MNRAS*, **473**, 5407
- Ménard, B., & Chelouche, D. 2009, *MNRAS*, **393**, 808
- Morrissey, P., Matuszewski, M., Martin, D. C., et al. 2018, *ApJ*, **864**, 93
- Murphy, M. 2016, UVES\_popler: POst-PipeLine Echelle Reduction software.  
<https://doi.org/10.5281/zenodo.56158>
- Murphy, M. T., Kacprzak, G. G., Savorgnan, G. A. D., & Carswell, R. F. 2019, *MNRAS*, **482**, 3458
- Muzahid, S., Kacprzak, G. G., Charlton, J. C., & Churchill, C. W. 2016, *ApJ*, **823**, 66
- Muzahid, S., Kacprzak, G. G., Churchill, C. W., et al. 2015, *ApJ*, **811**, 132
- Nelson, D., Pillepich, A., Springel, V., et al. 2019, *MNRAS*, **490**, 3234
- Nestor, D. B., Johnson, B. D., Wild, V., et al. 2011, *MNRAS*, **412**, 1559
- Nestor, D. B., Turnshek, D. A., Rao, S. M., & Quider, A. M. 2007, *ApJ*, **658**, 185
- Ng, M., Nielsen, N. M., Kacprzak, G. G., et al. 2019, *ApJ*, **886**, 66
- Nielsen, N. M., Churchill, C. W., & Kacprzak, G. G. 2013a, *ApJ*, **776**, 115
- Nielsen, N. M., Churchill, C. W., Kacprzak, G. G., & Murphy, M. T. 2013b, *ApJ*, **776**, 114
- Nielsen, N. M., Churchill, C. W., Kacprzak, G. G., Murphy, M. T., & Evans, J. L. 2015, *ApJ*, **812**, 83
- Nielsen, N. M., Kacprzak, G. G., Pointon, S. K., Churchill, C. W., & Murphy, M. T. 2018, *ApJ*, **869**, 153
- O’Meara, J. M., Lehner, N., Howk, J. C., et al. 2017, *AJ*, **154**, 114
- . 2015, *AJ*, **150**, 111
- Oppenheimer, B. D., & Davé, R. 2008, *MNRAS*, **387**, 577
- Oppenheimer, B. D., Davé, R., Kereš, D., et al. 2010, *MNRAS*, **406**, 2325
- Padilla, N., Lacerna, I., Lopez, S., et al. 2009, *MNRAS*, **395**, 1135
- Pearson, W. J., Wang, L., Alpaslan, M., et al. 2019, *A&A*, **631**, A51
- Peeples, M. S., Werk, J. K., Tumlinson, J., et al. 2014, *ApJ*, **786**, 54
- Peeples, M. S., Corlies, L., Tumlinson, J., et al. 2019, *ApJ*, **873**, 129
- Péroux, C., Nelson, D., van de Voort, F., et al. 2020, *MNRAS*
- Péroux, C., Rahmani, H., Arrigoni Battaia, F., & Augustin, R. 2018, *MNRAS*, **479**, L50
- Péroux, C., Quiret, S., Rahmani, H., et al. 2016, *MNRAS*, **457**, 903
- Péroux, C., Rahmani, H., Quiret, S., et al. 2017, *MNRAS*, **464**, 2053
- Pointon, S. K., Kacprzak, G. G., Nielsen, N. M., et al. 2020, *AJ*, **159**, 216
- . 2019, *ApJ*, **883**, 78
- Pointon, S. K., Nielsen, N. M., Kacprzak, G. G., et al. 2017, *ApJ*, **844**, 23
- Prochaska, J. X., Werk, J. K., Worseck, G., et al. 2017, *ApJ*, **837**, 169



- Rahmani, H., Péroux, C., Augustin, R., et al. 2018, *MNRAS*, **474**, 254
- Rakic, O., Schaye, J., Steidel, C. C., & Rudie, G. C. 2011, *MNRAS*, **414**, 3265
- Ribeiro, B., Le Fèvre, O., Cassata, P., et al. 2017, *A&A*, **608**, A16
- Rigby, J. R., Charlton, J. C., & Churchill, C. W. 2002, *ApJ*, **565**, 743
- Rodrigues, M., Hammer, F., Flores, H., Puech, M., & Athanassoula, E. 2017, *MNRAS*, **465**, 1157
- Rosenwasser, B., Muzahid, S., Charlton, J. C., et al. 2018, *MNRAS*, **476**, 2258
- Rubin, K. H. R., Prochaska, J. X., Koo, D. C., et al. 2014, *ApJ*, **794**, 156
- Rubin, K. H. R., Weiner, B. J., Koo, D. C., et al. 2010, *ApJ*, **719**, 1503
- Rudie, G. C., Steidel, C. C., Pettini, M., et al. 2019, *ApJ*, **885**, 61
- Rudie, G. C., Steidel, C. C., Trainor, R. F., et al. 2012, *ApJ*, **750**, 67
- Rupke, D. 2018, *Galaxies*, **6**, 138
- Rupke, D. S. N., Coil, A., Geach, J. E., et al. 2019, *Nature*, **574**, 643
- Sanders, R. L., Shapley, A. E., Kriek, M., et al. 2015, *ApJ*, **799**, 138
- Schroetter, I., Bouché, N., Wendt, M., et al. 2016, *ApJ*, **833**, 39
- Schroetter, I., Bouché, N. F., Zabl, J., et al. 2019, *MNRAS*, **490**, 4368
- Schweizer, F. 1978, in IAU Symposium, Vol. 77, Structure and Properties of Nearby Galaxies, ed. E. M. Berkhuysen & R. Wielebinski, 279
- Shapiro, K. L., Genzel, R., Förster Schreiber, N. M., et al. 2008, *ApJ*, **682**, 231
- Shapley, A. E., Steidel, C. C., Pettini, M., & Adelberger, K. L. 2003, *ApJ*, **588**, 65
- Shen, S., Madau, P., Guedes, J., et al. 2013, *ApJ*, **765**, 89
- Shibuya, T., Ouchi, M., Kubo, M., & Harikane, Y. 2016, *ApJ*, **821**, 72
- Simard, L., Willmer, C. N. A., Vogt, N. P., et al. 2002, *ApJS*, **142**, 1
- Simcoe, R. A., Sargent, W. L. W., Rauch, M., & Becker, G. 2006, *ApJ*, **637**, 648
- Simons, R. C., Kassin, S. A., Snyder, G. F., et al. 2019, *ApJ*, **874**, 59
- Sobral, D., & Matthee, J. 2019, *A&A*, **623**, A157
- Speagle, J. S., Steinhardt, C. L., Capak, P. L., & Silverman, J. D. 2014, *ApJS*, **214**, 15
- Steidel, C. C., Erb, D. K., Shapley, A. E., et al. 2010, *ApJ*, **717**, 289
- Steidel, C. C., Rudie, G. C., Strom, A. L., et al. 2014, *ApJ*, **795**, 165
- Stern, J., Hennawi, J. F., Prochaska, J. X., & Werk, J. K. 2016, *ApJ*, **830**, 87
- Stewart, K. R., Brooks, A. M., Bullock, J. S., et al. 2013, *ApJ*, **769**, 74
- Stewart, K. R., Kaufmann, T., Bullock, J. S., et al. 2011, *ApJ*, **738**, 39
- Stewart, K. R., Maller, A. H., Oñorbe, J., et al. 2017, *ApJ*, **843**, 47
- Sugahara, Y., Ouchi, M., Lin, L., et al. 2017, *ApJ*, **850**, 51
- Thom, C., Werk, J. K., Tumlinson, J., et al. 2011, *ApJ*, **736**, 1
- Thornley, M. D., Schreiber, N. M. F., Lutz, D., et al. 2000, *ApJ*, **539**, 641
- Trainor, R. F., Steidel, C. C., Strom, A. L., & Rudie, G. C. 2015, *ApJ*, **809**, 89
- Tripp, T. M., Meiring, J. D., Prochaska, J. X., et al. 2011, *Science*, **334**, 952
- Tumlinson, J., Peeples, M. S., & Werk, J. K. 2017, *Annual Review of Astronomy and Astrophysics*, **55**, 389
- Tumlinson, J., Thom, C., Werk, J. K., et al. 2011, *Science*, **334**, 948
- . 2013, *ApJ*, **777**, 59
- Turner, M. L., Schaye, J., Crain, R. A., et al. 2017, *MNRAS*, **471**, 690
- Turner, M. L., Schaye, J., Steidel, C. C., Rudie, G. C., & Strom, A. L. 2014, *MNRAS*, **445**, 794
- . 2015, *MNRAS*, **450**, 2067
- van de Voort, F., & Schaye, J. 2012, *MNRAS*, **423**, 2991
- van de Voort, F., Schaye, J., Booth, C. M., & Dalla Vecchia, C. 2011, *MNRAS*, **415**, 2782
- van der Wel, A., Franx, M., van Dokkum, P. G., et al. 2014, *ApJ*, **788**, 28
- Veilleux, S., Cecil, G., & Bland-Hawthorn, J. 2005, *ARA&A*, **43**, 769
- Verhamme, A., Orlitová, I., Schaerer, D., et al. 2017, *A&A*, **597**, A13
- Verhamme, A., Garel, T., Ventou, E., et al. 2018, *MNRAS*, **478**, L60
- Weiner, B. J., Coil, A. L., Prochaska, J. X., et al. 2009, *ApJ*, **692**, 187
- Wendt, M., Bouché, N. F., Zabl, J., Schroetter, I., & Muzahid, S. 2020, arXiv e-prints, [arXiv:2009.08464](https://arxiv.org/abs/2009.08464)
- Werk, J. K., Prochaska, J. X., Thom, C., et al. 2013, *ApJS*, **204**, 17
- Werk, J. K., Prochaska, J. X., Tumlinson, J., et al. 2014, *ApJ*, **792**, 8
- Whiting, M. T., Webster, R. L., & Francis, P. J. 2006, *MNRAS*, **368**, 341
- Wisnioski, E., Förster Schreiber, N. M., Wuyts, S., et al. 2015, *ApJ*, **799**, 209
- Wotta, C. B., Lehner, N., Howk, J. C., et al. 2019, *ApJ*, **872**, 81
- Wotta, C. B., Lehner, N., Howk, J. C., O’Meara, J. M., & Prochaska, J. X. 2016, *ApJ*, **831**, 95
- Xue, R., Lee, K.-S., Dey, A., et al. 2017, *ApJ*, **837**, 172
- Yun, M. S., Ho, P. T. P., & Lo, K. Y. 1994, *Nature*, **372**, 530

Zabl, J., Bouché, N. F., Schroetter, I., et al. 2019, [MNRAS](#),  
485, 1961

Zahedy, F. S., Chen, H.-W., Johnson, S. D., et al. 2019a,  
[MNRAS](#), 484, 2257

Zahedy, F. S., Rauch, M., Chen, H.-W., et al. 2019b,  
[MNRAS](#), 486, 1392

Zheng, Z., & Miralda-Escudé, J. 2002, [ApJ](#), 578, 33

Zhu, G., & Ménard, B. 2013, [ApJ](#), 770, 130